THESIS FOR THE DEGREE OF LICENTIATE OF TECHNOLOGY

Strong light-matter coupling: from traditional to cavity-free polaritons

Adriana Canales Ramos

Department of Physics
Chalmers University of Technology
Göteborg, Sweden, 2021

STRONG LIGHT-MATTER COUPLING: FROM TRADITIONAL TO CAVITY-FREE POLARITONS

Adriana Canales Ramos

Division of Nano- and Biophysics
Department of Physics
Chalmers University of Technology
SE-412 96 Göteborg
Sweden

Cover:
Top: Light reflected from a 60 *nm thick slab of* MoS_2*, with magnification to its atomic structure. Left: picture of the Fourier plane of the light reflected from the slab, which expands the angular information. Bottom right: the spectral resolution of the showed area in the Fourier plane, showing the angular dispersion of cavity-free polaritons above and below the light-line.*

Printed in Sweden by
Chalmers digital printing
Chalmers Tekniska Högskola
Göteborg, Sweden, 2021

CHALMERS UNIVERSITY OF TECHNOLOGY

Department of Physics

Strong light-matter coupling: from traditional to cavity-free polaritons

Adriana Canales Ramos

Abstract

Polaritons are formed when light and matter interact strongly. For this to occur, an optical mode and a material transition mode must exchange energy faster than the dissipation rates of the components. As a result, the polaritons have their own energy levels and dissipation rates. Polaritons have shown the ability to change material properties like photophysics, chemical reaction rates, transport, etc.

Most of the studies on strong coupling use an external cavity. Such platforms form what here are called *traditional* polaritons. To maximize the coupling, the external cavity has to be tailored to match the, usually fixed, material transition properties. Moreover, often such a cavity is made of two metallic mirrors that restrict the access to the material.

The results in this thesis are divided in two parts. The first part is devoted to traditional polaritons in a microcavity-plasmon coupling platform. The versatility of the platform allows to tune the plasmon characteristics to achieve strong or ultrastrong coupling at room temperature.

The second part is dedicated to *cavity-free* or self-hybridized polaritons. Here, it is shown that polaritons can be sustained in simple structures as slabs, cylinders and spheres, by using that the material sustaining a transition resonance can also sustain its own optical modes. Very small structures do not sustain optical modes in resonance with the transitions, giving rise to a minimal critical size for polaritons to exist. Moreover, the coupling strength seems to be limited by the macroscopic optical properties of the material.

These results can guide the community to quickly realize which materials can be used to form polaritons, as well as, to find polaritons in simpler structures. Since the structures are not embedded in the cavity, a window of opportunity is open for applications and further studies on the impact of polaritons on material properties.

Keywords: Polaritonic states, strong coupling, ultrastrong coupling, cavity-free polaritons, Lorentz resonances, Mie modes, Fabry-Pérot modes, 2D-atomic crystals.

List of publications

The following papers are included in this thesis:

I **Abundance of cavity-free polaritonic states in resonant materials and nanostructures**
Adriana Canales, Denis G. Baranov, Tomasz J. Antosiewicz & Timur Shegai
The Journal of Chemical Physics **154**, 024701 (2021).

Declaration of author contributions:

I: I performed calculations, lead the discussions and co-wrote the manuscript.

Supplementary papers not included in this thesis:

S.I **Collective Strong Light-Matter Coupling in Hierarchical Microcavity-Plasmon-Exciton Systems**
Ankit Bisht, Jorge Cuadra, Martin Wersäll, Adriana Canales, Tomasz J. Antosiewicz & Timur Shegai
Nano Letters **19(1)**, 189 – 196 (2019).

My contribution: I assisted in optical measurements and fabrication of the samples, and took part in discussions.

S.II **Ultrastrong coupling between nanoparticle plasmons and cavity photons at ambient conditions**
Denis G. Baranov, Battulga Munkhbat, Elena Zhukova, Ankit Bisht, Adriana Canales, Benjamin Rousseaux, Göran Johansson, Tomasz J. Antosiewicz & Timur Shegai
Nature Communications **11**, 2715 (2020).

My contribution: I assisted on the first samples for the project, the final theory analysis and provided feedback on the manuscript.

S.III **Casimir microcavities for tunable self-assembled polaritons**
Battulga Munkhbat, Adriana Canales, Betul Küçüköz, Denis G. Baranov & Timur Shegai
Nature **597**, 214–219 (2021).

My contribution: I lead the Fourier imaging measurements, assisted on optical characterization of the samples, took part on the discussions, and provided feedback on the manuscript.

Acknowledgements

What a journey it has been! There is not enough space to thank all the people that have inspired me and helped me along the way, but here is a short list.

First, I would like to thank my supervisor, Timur Shegai, for giving me the opportunity to be here and for making this work possible. Thank you for the infinite flow of ideas and suggestions. Your enthusiasm and passion are contagious! More importantly, thank you for walking alongside me during my recovery.

Mikael Käll, my examiner. Thank you for the scientific discussions and for always giving me valuable advice. I should listen to you more often. Also, thank you for showing me that it is possible to have multiple passions and succeed in Academia.

Denis Baranov, I am very grateful for your support and jumping in the boat as co-supervisor. The work presented here would have taken me a few centuries without your constant help and guidance. Thank you for listening to me when I was at my lowest and sharing great advice. You are a true role model. I can't wait to follow the rest of your brilliant career.

Tomasz Antosiewicz, my co-supervisor. Thank you for your infinite patience when answering my questions, for being so careful and for humbly sharing your knowledge with me. Of course, also for all the FDTD calculations you have performed for this work and for the detail with which you revised this text.

Betül Kücüköz, my amazing (perfectly nice) office mate and dear friend. There are not words to express my gratitude. Thank you for sharing with me all the laughter, disappointment, enthusiasm, panic, excitement, tears and happiness. We are a great team, going at the same speed and learning together. There was no person happier than me when you got your new position. Everything is awesome!

Ankit Bisht, the best teacher! Thank you for sharing with me your wonder and curiosity, for introducing me to the nanofab world and optical measurements. I inherited your habits. Thank you for your constant help even when you are not anymore part of the group. I'm so lucky that you didn't go so far. Of course, thanks for all the life discussions!

Daniel Andrén, the success story! Thank you for guiding me in the process of becoming a PhD student, for teaching me E-beam, for sharing your wisdom, your realism and enthusiasm, and for being a great person. For sharing with me your beautiful science. You are an Ironman! See you in the water!

Oleg Kotov, thank you for the calculations that inspired my best measurements so far. They are a true beauty, and I am happy we get the pleasure to share them with the world.

Battulga Munkhbat, thank you for all the AFM measurements and constant help around the lab. Good luck with the new position.

Martin Wersäll and Michael Stührenberg, you walked the path before me, and

I am very lucky to have your insight and advice. Thank you for training me and re-training me on SEM. Also, for all the good discussions, both about science and life.

Luis Martins, thank you for all your help and discussions when I was figuring out the Fourier plane, even when you had no idea what I was doing (and back then, neither did I).

Javier Tello, I think we are finally understanding what we are doing (or not). Thank you for all those good discussions, they always make me feel like a grown up scientist.

Thanks to all the members of the ex-BNP and new NBP division. Particularly to Steve, Pantea, Alexander, Katya, Hana, Mahdi, Emelie and Ximin for all the laugher and fika together.

People from the DS, FFF and CPPC boards, thank you for making such important work and giving me the chance to make a difference. It is always a pleasure to discuss and work together.

I am deeply grateful for all the help I received during my sick leave. Thanks to Pe3, Moyra, Deborah, Eva Olsson and once more, to Timur, for helping me during my recovery. Thanks to *La bandita*: Martín, Lau, Karen, Dani, Agin, Simon, Emi and Ana for being a constant source of happiness and support. Mil gracias!

Finally, I am grateful to my parents and family for always supporting me and encouraging me at a distance in all my crazy projects, including this one. Especially to Sean, mi Chonis, my team, my home, tusen takk!

Adriana Canales Ramos

Göteborg, 2021/09/03

Contents

Chapter 1

Introduction

The interaction between light and matter allows us to see and understand the world. Our understanding of the interaction has improved over time and applications have arisen. Nowadays, light is commonly used as a tool to study the properties of materials through different spectroscopic techniques. But also, light can change material properties permanently via photobleaching, or by reshaping them with lasers. Moreover, the spontaneous emission of materials has been tailored and used for making biosensors and lasers. These applications involve irreversible energy exchange between the light and the material.

Strong-light matter coupling happens when matter and light exchange energy reversibly. Let us imagine a material with a transition between two energy levels placed inside an optical cavity. Intuitively, the cavity confines photons inside long enough for them to be absorbed by the material. Their absorption generates a transition from a lower energy level to a higher one. The element of matter is then in the excited state. After a while, let's think that the material goes back to the lower energy state by emitting a photon back to the cavity. There the photon is confined until it is reabsorbed by the material, and the cycle repeats. When this energy exchange, between the cavity and the transition, is faster than the rate at which photons escape the cavity and the rate at which the material losses energy to the environment, the two components become indistinguishable. A light-matter hybrid is created. This new quasi-particle is called a *polariton*.

Polaritons have their own energy levels. This means that the energy levels of the material can be changed by putting it between two mirrors (optical cavity). Moreover, the material recovers its original energy levels if the mirrors disappear. This triggered the interest of the community to look for applications of polaritons to tailor material properties. Studies have shown changes in photophysics [1–3], chemical reaction rates [4, 5], charge transport [6], energy transfer [7], among others [8, 9]. Polaritons are also coherent, which has made them attractive for quantum information applications. Even more so, condensation of polaritons has been achieved in different platforms [10, 11].

Most of the aforementioned studies were done by tailoring an external cavity, such that its electromagnetic field overlaps, both in space and energy, with the transition between two energy levels of a chosen material. The external cavity can be made of two metallic mirrors, or Bragg mirrors, a photonic crystal, a plasmonic particle, etc. The use of these external cavities produces what in this thesis are called *traditional* polaritons. Chapter 3 is devoted to discussing this kind of polaritons.

The term *polariton* was proposed by Hopfield [12–14] in a slightly different situation than the one described above. He studied the interaction of an electromagnetic

plane wave with collective excitations, as excitons or phonons, in bulk materials. Throughout this text, this is what is referred to as *bulk* polaritons. They will be described in Chapter 4.

The existence of bulk polaritons brings into question the role of the external cavity in *traditional* polaritons. Let us say that their role is to confine the optical mode. In that case, it is known that materials can also sustain different optical resonances depending on their shape [15]. Some of those resonances are covered in Chapter 2.2. Thus by reshaping the material into simple structures it is possible to use the optical modes in the same material to reach strong coupling. This allows to avoid using an external cavity. Even though the idea of coupling a material resonance to an optical resonance sustained by the same reshaped material is not new [16–18], the appended paper shows that *cavity-free* polaritons are more general and common than previously thought, existing naturally even in simple structures, such as water droplets.

The structure of this thesis is as follows. First, the macroscopic optical response of materials is revised, which is needed for the following Chapters. There is an emphasis on the permittivity for different materials used through the text such as water, 2D-atomic crystals (MoS_2 and hBN) and metals. From the latter, plasmons are introduced, which are collective free-electron oscillations. At the end of section 2.1, the changes in the total optical response by stacking materials with different permittivities are discussed. It is shown there that a simple structure formed by a few nm thick layer of a 2D-atomic crystal (MoS_2), on a glass substrate, can achieve perfect absorption of light.

The second part of Chapter 2, is devoted to the optical resonances in dielectric structures of different geometries: slabs, cylinders and spheres. These optical resonances are then used in Chapter 4 to strongly couple collective excitations of a material to the optical resonances sustained by the same material.

Chapter 3 focuses on the theory of strong and ultrastrong coupling. In the latter, the coupling strength is on the order of the transition energy. A specific example of *traditional* polaritons is considered by coupling plasmons to microcavity photons. This platform allows to achieve strong and ultrastrong coupling at room temperature by tuning the plasmonic nanodisk array properties.

Chapter 4 starts with a description of *Bulk* polaritons. Particularly, showing the dispersion and trajectories of the resonant states in the complex plane for different coupling regimes. Then, *cavity-free* polaritons are shown in different geometries. This part includes a summary of the results of the appended paper, additional calculations, recent works by other groups with exciting results, and our recent experimental results in polaritonic MoS_2 slabs.

Chapter 5 summarizes the methods used through the thesis. Including details on the theoretical calculations, the fabrication methods and the optical characterization techniques. Especially, the Fourier spectroscopy technique for measuring dispersion at the nano-micrometer scale.

Finally, Chapter 6 gives a summary of the results presented in the thesis. Also, there is an outlook for future research, mainly on *cavity-free* polaritons. There the appended paper is put into the context of the current interest of the strong coupling community.

Chapter 2

Light-matter interactions

The interaction between light and matter allows us to see, study and understand the world. In this Chapter, a macroscopic approach to the response of materials to light is given.

The chapter is divided in two main sections. The first one focuses on electronic, vibrational, excitonic, or phononic resonances in materials, mainly through using the Lorentz model to describe the material permittivities, ε. Specific examples of ε are given for water, 2D-atomic crystals and metals. The discussion on metals includes a description of plasmons. Finally, an application of tailoring the optical response is described by showing perfect absorption of light in a few nm thick 2D MoS_2.

The second part of the chapter describes optical resonances in simple structures as slabs, cylinders and spheres. Later in the text, both parts will be used together, to investigate confined light interacting strongly with a resonance of the material.

2.1 Optical properties of matter

Light is an oscillating electromagnetic wave with electric and magnetic field. The electric field of a plane wave in vacuum evolves as $\mathbf{E}(\mathbf{r},t) = \mathcal{E}e^{\mathrm{i}k\cdot\mathbf{r}-\mathrm{i}\omega t}$, where $\mathbf{r}$ is the direction of propagation, $\mathbf{k}$ the wave vector and ω the angular frequency. The angular frequency is related to a photon with energy $E = \hbar\omega$ in electron volts, eV[1]. In vacuum, the relation between the wave vector and the angular frequency is simply, $k = |\mathbf{k}| = \omega/c = \frac{2\pi}{\lambda}$, with $c = 1/\sqrt{\varepsilon_0\mu_0}$. This is the dispersion relation of light propagating in vacuum. Throughout the text, it is referred to as the *light-line* in vacuum.

Let us consider a plane wave propagating through a material. The electrons will be displaced in response to $\mathbf{E}$ and to the neighboring atoms response. This response is the polarizability, $\mathbf{P}$. As a result, in linear optics[2], the plane wave is described by the electric displacement:

$$\mathbf{D} = \varepsilon_0\mathbf{E} + \mathbf{P} = \varepsilon_0\mathbf{E} + \varepsilon_0\chi\mathbf{E}\,, \tag{2.1}$$

where ε_0, is the permittivity in vacuum and χ the susceptibility of the material. It is possible to rewrite the displacement in terms of the relative permittivity in the

[1] For simplicity $\hbar\omega$ is shortened to ω in the text.

[2] Nonlinearities become important when the intensity of the field $\mathbf{E}$ increases. In which case, higher order values of the susceptibility, χ^n, become important. Such effects are beyond the scope of this thesis, but more information can be found in [19].

material as $\mathbf{D} = \varepsilon_0\varepsilon\mathbf{E}$. Thus, the response to the plane wave is contained in the complex relative permittivity of the material $\varepsilon = \varepsilon' + \mathrm{i}\varepsilon''$. The response of the material to incoming light usually varies with frequency of light, ω, meaning that they are *dispersive*. The dispersion is considered in the dielectric *function*, $\varepsilon(\omega)$. Moreover, for anisotropic materials the permittivity is a tensor [20], but this is beyond the scope of this thesis.

A useful macroscopic quantity related to the permittivity is the complex refractive index, $\tilde{n} = n + \mathrm{i}\kappa$. The real part, n, is related to the velocity of light in the material $v = c/n$. Thus, the light-line in the material is $\omega = ck/n$. The imaginary part, κ, is the extinction coefficient which is related to the absorption in the material. The permittivity is obtained from the refractive index via[3] $\tilde{n}^2 = \varepsilon$ [19].

In a *lossy* material the light dispersion ($\omega = ck/n$) can be considered in two scenarios:

(i) $\tilde{k}$ being a complex number helps to understand the spacial decay of the wave. For example, $\mathbf{k} = \hat{x}k_x + \hat{z}\mathrm{i}k_z$ describes an evanescent wave that exponentially decays in the positive z direction.

(ii) $\tilde{\omega}\omega - \mathrm{i}\gamma/2$ being complex gives a description of decay in time. In which case a wave with energy, $E = \hbar\omega$ decays at a rate given by γ.

Throughout this text the second scenario is considered to describe life-times more than the spatial decay.

2.1.1 Drude-Lorentz model

A useful model to classically describe ε is Lorentz model [19, 20], where light induces oscillations of the bound charges of the material. Let us consider an isotropic material with a density of electrons (ρ) that oscillate around the ions with a frequency ω_0. Then the polarizability, $\mathbf{P} = -ex$, evolves in time as

$$\ddot{\mathbf{P}}(t) + \gamma\dot{\mathbf{P}}(t) + \omega_0^2\mathbf{P} = f\frac{\rho e^2}{m_e}\varepsilon_0\mathbf{E}(t)\ , \tag{2.2}$$

where, m_e is the electron mass, e its charge, and γ is the damping frequency. To account for the fact that different resonances show experimentally different absorption, an oscillator strength, f is included phenomenologically in this classical model. Equation 2.2 is solved by performing a Fourier transform, obtaining

$$\mathbf{P}(\omega) = f\frac{\rho e^2/m_e}{\omega_0^2 - \omega^2 - \mathrm{i}\gamma\omega}\varepsilon_0\mathbf{E}(\omega)\ . \tag{2.3}$$

Assuming a homogeneous and isotropic material, $\mathbf{P}(\omega) = \varepsilon_0\chi\mathbf{E} = \varepsilon_0(\varepsilon - 1)\mathbf{E}$. Then the permittivity can be written as,

$$\varepsilon(\omega) = 1 + f\frac{\omega_p^2}{\omega_0^2 - \omega^2 - \mathrm{i}\gamma\omega}\ , \tag{2.4}$$

where $\omega_p = \sqrt{\rho e^2/m_e\varepsilon_0}$ is the plasma frequency and f is the oscillator strength of the resonance, which is related to the efficiency of the interaction between the electric field and the electronic or vibrational transition.

[3] Through the text, nonmagnetic media is considered, $\mu = 1$.

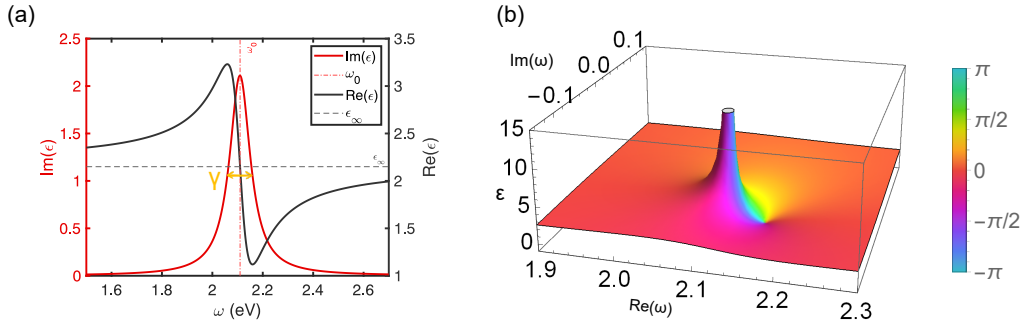

FIGURE 2.1: Permittivity of a Lorentzian fit of J-aggregates [21] (a) Real and imaginary part of $\epsilon(\omega)$ for real frequencies. The FWHM (yellow) is given by γ. (b) Same Lorentzian permittivity in the complex-ω plane, depicting the pole at $\omega_0 - i\gamma/2$.

Equation 2.4 considers only a single resonance. However, in a real material several resonances contribute to the total optical response (see equation 5.9). The background permittivity is included To account for the higher energy resonances [19]:

$$\varepsilon_r(\omega) = \varepsilon_\infty + f\frac{\omega_p^2}{\omega_0^2 - \omega^2 - i\gamma\omega} \,. \tag{2.5}$$

Figure 2.1(a) shows the real and imaginary parts of the complex permittivity of J-aggregates, with $\omega_0 = 2.11$ eV, $\gamma = 0.1$ eV and $\varepsilon_\infty = 2.15$ eV [21]. If we plot the same permittivity in the complex-ω plane we can see that equation 2.5 has a pole, $\varepsilon(\omega) \to \infty$, when $\omega = \omega_0 - i\gamma/2$.

2.1.2 Permittivities of real materials

In different materials and at various energies, the nature of the resonances described by $\varepsilon(\omega)$ may be different. Some resonances originate from electronic transitions, vibrational transitions or even excitons [19, 20]. Various examples are considered here.

Water permittivity

Let us start with a familiar example: water. Figure 2.2(a) shows the complex permittivity of water in the infrared (IR) spectral region. The resonances are given by different vibrations. For example, the O-H stretch gives the resonance around 0.42 eV and around 0.2 eV due to O-H scissoring. The Lorentzian fit of the former transition is $\omega_0 = 0.42$ eV, $\gamma = 0.048$ eV and $\varepsilon_\infty = 1.75$ eV.

Previously, it was discussed that f in the Lorentz model was a phenomenological fit. Due to the difference in amplitudes, it is easy to see (figure 2.2(a)) that the resonance in 0.42 eV has higher oscillator strength than the one in 0.2 eV. Such value can be obtained from the fit (figure 2.2(b)). In this case, $f\omega_P^2 = 0.018$ eV^2. It is also possible to express the oscillator strength in terms of microscopic parameters by

$$f = 2\frac{m_e\omega_0}{\varepsilon_0\hbar}|\mu|^2 \,, \tag{2.6}$$

where μ is the transition dipole moment of the transition. This expression will come handy in the following chapter.

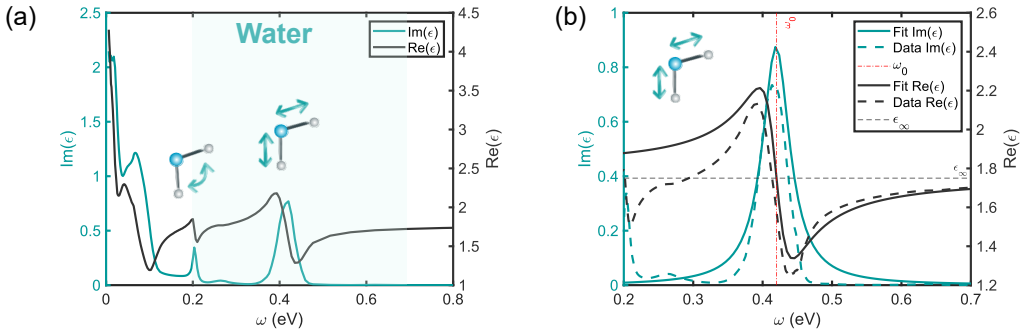

FIGURE 2.2: Permittivity of water. (a) Several vibrational resonances in experimental data for the permittivity of water [22, 23]. (b) Experimental data and Lorentz fit for the O-H stretch in water.

2D-atomically thin van der Waals materials

Van der Waals (VdWs) bulk crystals are layered materials that can be easily separated by mechanical exfoliation due to the weak VdWs interaction between layers. Therefore, it is possible to obtain 2D-atomically thin layers similar to graphene. For that reason, they have attracted a lot of attention in the last decades. As a result, several materials with a broad range of characteristics have been studied [24, 25], including their potential to stack them to engineer their properties [26].

The discussion here is restricted to the optical properties of two very studied layered materials: hexagonal-boron nitride (hBN) and MoS_2 [26].

- **Hexagonal-boron nitride**

  Due to its similarity to graphene (figure 2.3(a)) it has been heavily used as a *perfect* substrate to enhance properties of other 2D-atomic crystals, such as conductivity. It is a very inert insulator with a high bandgap (6 eV) [27].

  Nonetheless, it has interesting optical properties of its own in the infrared (IR) part of the spectra. HBN is highly anisotropic (the permittivity in-plane is very different from the permittivity out-of-plane). Thus, the normal lattice vibrational resonances (optical phonons) are anisotropic as well, giving rise to two distinct phonon branches one around 169 meV (in-plane) and one around 95 meV (out-of-plane) [28].

  Finally, a Lorentzian fit to the experimental data (figure 2.3(a)) shows the large oscillator strength[4] of the resonance and its high background permittivity. Such high refractive index in the IR allows the material to easily sustain optical resonances, as described in section 2.2.

- **MoS_2**

  Bulk molybdenum disulfide, MoS_2, is an indirect band-gap semiconductor part of the *Transition Metal Dichalcogenides*[5] (TMDs) family. The bulk material

[4] Large in comparison to most materials (see Methods table 5.1).

[5] TMDs are semiconductors of the type MX_2, where M is a transition metal atom (e.g., Mo, W or Ta) and X is a chalcogen atom (e.g., S, Se or Te) [25].

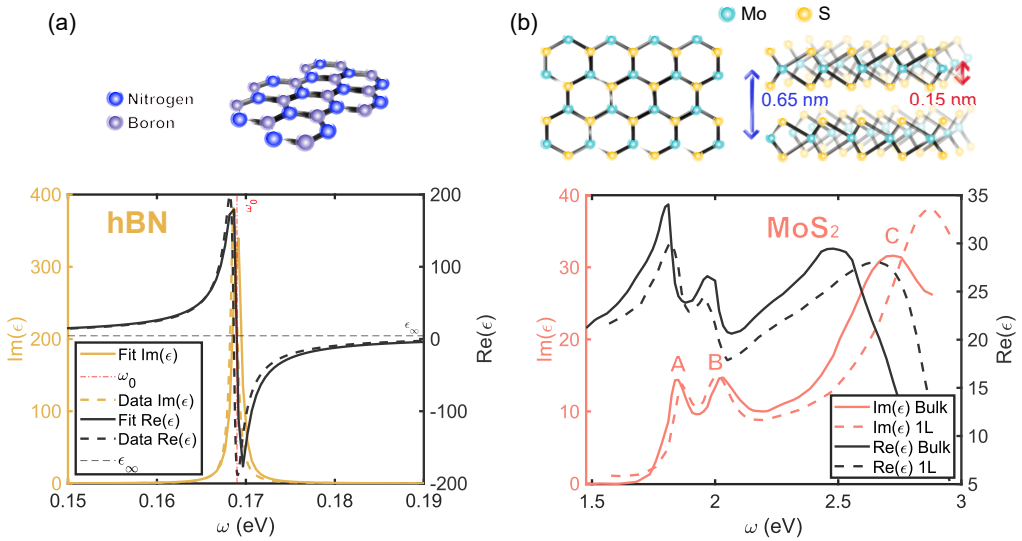

FIGURE 2.3: Permittivity of 2D-atomic crystals. (a) Top: schema of hBN 2D-atomic structure. Bottom: Bulk *in-plane* permittivity of hBN with Lorentzian fit. (b) Top: schema of MoS_2 2D-atomic structure, top view of a monolayer (left) and side view of a bilayer (right). On the bottom, permittivity of bulk and monolayer (data from [29]).

consists of 3-atom thick layers stacked[6] together via van der Waals interactions as shown schematically in figure 2.3(b).

The optical response of bulk and monolayer MoS_2 are contained in the dielectric function, shown in figure 2.3(b) (data from [29]). The observed absorption in the $\mathrm{Im}(\varepsilon)$ is given by interlayer excitons[7]. The excitons have an energy shift from monolayer to bulk, due to the change in relaxation paths when increasing the number of layers [29]. Also, in the bulk, TMDs also have high background refractive index in the visible range.

One of the most important optical properties of monolayers is the appearance of photoluminescence from the exciton recombination [32], because of the change from indirect (bulk crystal) to direct band gap (monolayer). This is the most efficient way of identifying MoS_2 monolayers. Other methods have been used to identify different number of layers, such as AFM and Raman microscopy among others [33].

The case of metals: plasmons

Equation 2.5 considers electrons bounded to ions. The Drude model, is used when the electrons are free, as is the case in a conductive material. Thus, the resonance frequency in the Lorentzian (equation 2.4) is set to zero, $\omega_0 = 0$.

[6]The stacking configuration of the atoms in a single layer (determines the phase, shown in the figure is 2H MoS_2). For stacking of several layers AB stacking is the stable form for the 2H phase [30]. The stacking is important for the thickness determination, but also for properties as second harmonic generation and transport. This is beyond the scope of this thesis, for a better description see [25, 30, 31]

[7]Tightly bound electron-hole pairs. They are usually present in semiconductors, but screened by other charges. TMDs have particularly high binding energies of excitons and are stable even in room temperature.

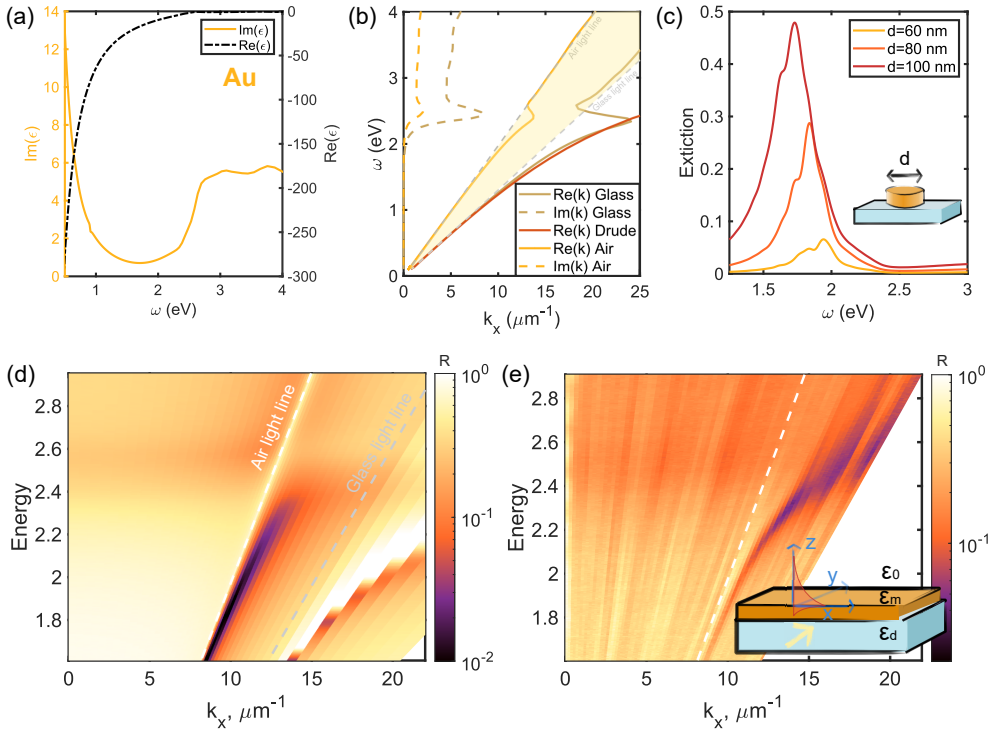

FIGURE 2.4: Plasmons in gold. (a) Experimental data of ε_{Au} [34]. (b) Dispersion of the surface plasmon in glass-metal and air-metal interfaces. (c) FDTD calculations of the LSPR of Au disks with different diameters and height of 20 nm. (d) Reflectively calculation, by Transfer Matrix Method [35], of a 35 nm thick infinite Au layer on top of glass showing the SPP dispersion. (e) Reflectivity measurement of the SPP of a 35 nm thick and 30 μm side length.

$$\varepsilon(\omega) = \varepsilon_\infty - \frac{\omega_p^2}{\omega^2 + \mathrm{i}\gamma\omega} \,. \tag{2.7}$$

In this case the physical origin of the damping is given by the electrons collisions frequency in the metal, γ. Figure 2.4(a) shows the experimental permittivity of Au. The first thing to note is that $\mathrm{Re}(\epsilon) < 0$, which means that the electrons in the material reflect the incident field. Thus, Au is a great mirror for the IR region, but not in the UV because $\mathrm{Im}(\epsilon)$ absorbs for $\omega > 2eV$ due to the interband transitions. In this spectral range a mix of Drude and Lorentz is required for a better description of its permittivity [20, 36].

Moreover, a metal sustains *longitudinal* collective electron oscillations when $\varepsilon(k,\omega) = 0$. In the low damping $\gamma \ll \omega$ regime of equation 2.7 and in the free electron model $\varepsilon_\infty \to 1$, this means that $\varepsilon(\omega) = 1 - \omega_P^2/\omega^2$. Then *volume plasmons* can be excited when $\omega = \omega_P$, but not by light because they are longitudinal waves.

Nevertheless, by placing a metal on top of a dielectric material, *surface plasmon polaritons* (SPPs) can be excited with TM-polarized waves ($E_z(z) \neq 0$) at the interface between them [36]. SPPs are collective electron oscillations coupled to the incident electromagnetic field. In this case, the dispersion equation depends on both the permittivity of the metal, ε_m, and the dielectric, ε_d

$$k_{SPP} = k_0 \sqrt{\frac{\varepsilon_m \varepsilon_d}{\varepsilon_m + \varepsilon_d}} \,. \tag{2.8}$$

Figure 2.4(b) shows the dispersion (equation 2.8) of SPPs at the interface between gold, $\varepsilon_m = \varepsilon_{Au}$ in 2.4(a), and two different dielectrics, glass ($\varepsilon_d = n_d^2 = 1.51^2$) and air ($\varepsilon_d = 1$). The SPP dispersion at the Au/air interface is limited by the light-line of air, meaning that SPPs cannot be excited with incoming light from air. In order to excite and measure them one solution is to use a dielectric material with a larger permittivity, $\varepsilon > 1$, to provide enough momentum (parallel to the interface, along x in this case) to the photons such that $k_x = k\varepsilon \sin(\theta) = k_{SPP}$. That high index material can be glass to give access to the area shadowed in yellow in Figure 2.4(b).

Figure 2.4(e) shows a reflectivity measurement of a surface plasmon at a 35 nm thick Au film/air interface in Kretschmann configuration. Such configuration allows to measure the air-metal SPP by using the glass permittivity (substrate) at angles higher that the critical angle for total internal reflection [36], see Methods 5.3.1 for experimental details. To measure the SPP at the Au/glass interface a material with higher refractive index than glass is required to give the incoming photons enough in-plane momentum. Nevertheless, it is visible in the calculation of the reflectivity of the same system (35 nm of Au on top of glass) in a Transfer Matrix Method (TMM)[35] calculation (see figure 2.4(d)) because the incident in-plane momentum, k_x, can be arbitrarily large.

On another note, *localized surface plasmon resonances* (LSPRs) can be excited simply with light incoming from air. In this case, the free electrons in a particle oscillate in response to the incoming electric field, enhancing the total optical response, but constrained to the particle [36].

To see the reason of the field enhancement we can consider a sphere of radius a. The dipole moment induced by the field is $\mathbf{p} = \varepsilon_d \alpha \mathbf{E}_0$. To calculate the polarizability, α we consider the *quasi-static approximation*, $d \ll \lambda$, such that $\mathbf{E}$ is constant over the full particle [36],

$$\alpha(\omega) = \frac{4\pi a^3}{3} \frac{\varepsilon_m(\omega) - \varepsilon_d}{\varepsilon_m(\omega) + 2\varepsilon_d} \,. \tag{2.9}$$

When the denominator approaches 0, the polarizability has a resonance. Thus, if $\mathrm{Im}(\varepsilon_m)$ varies slowly around the resonance frequency, this is reduced to $\mathrm{Re}(\varepsilon_m) = -2\varepsilon_d$. Thus, the medium surrounding the particle is key for the resonance frequency. Also, $\mathrm{Re}(\varepsilon_m) < 0$, implies the need for a metal. This field enhancement by small metallic particles has been highly exploited for sensing with metallic nanoparticles [36].

The LSPR is not limited to a metallic particle of spherical shape, however, analytical calculations of the response of non-spherical particles are more challenging [37]. The following chapter uses the LSPRs in metallic nanodisks for strong coupling. The disks can be approximated by an oblate spheroid to obtain an analytical description of α, which allows to approximate the optical response of a single nanodisk [38]. Nevertheless, for a more accurate calculation of the extinction cross section of nanodisk arrays numerical methods such as FDTD can be used. Figure 2.4(c) shows such calculations for infinite periodic arrays of Au nanodisks 20 nm in height with a 300 nm pitch between particles (center to center) for different nanodisk diameters. The various diameters allow to tune the frequency of the resonance.

Here, we have revised plasmonic resonances that will be very useful in the following chapter.This section also highlighted the importance of the interaction of

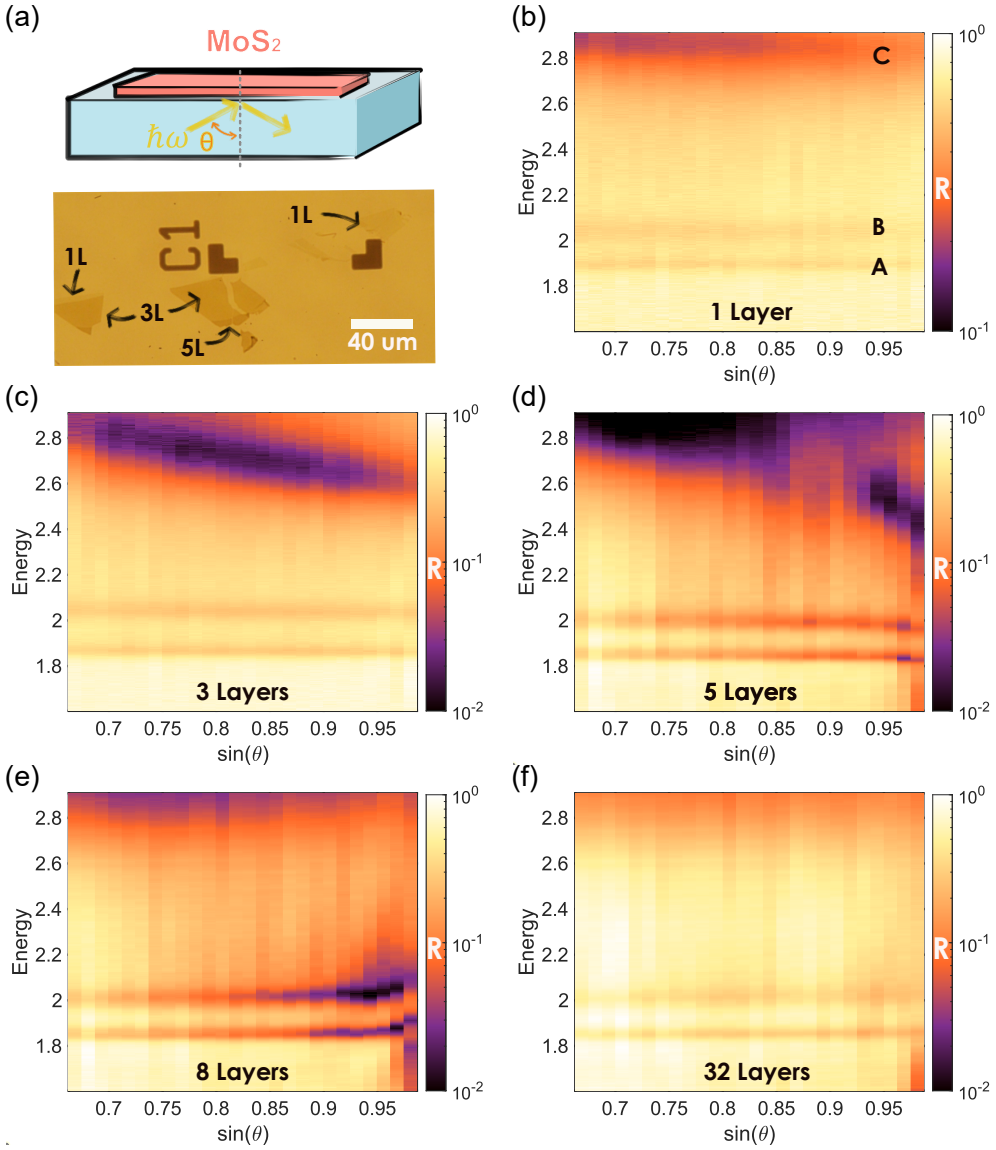

FIGURE 2.5: Perfect absorption in MoS_2 layers of TE polarized light. (a) Top: schema of the sample of a few layers of MoS_2 on glass with incoming light at high angles. Bottom: Bright field of the MoS_2 flakes in transmission. Reflectivity below the light-line of MoS_2 (b) monolayer (note the difference in color scale from the rest of the plots), (c) 3 Layers (d) 5 layers (e) 8 layers and (f) 32 layers.

materials with different permittivities to tailor the total optical response. The following section will discuss further the interesting optical response that arises even in very thin layers of materials.

2.1.3 Perfect absorption in thin MoS_2 layers

Above it was described that different permittivities and shapes can change the total optical response of a structure. An intriguing and pursued optical phenomenon has been to tailor a structure that can fully absorb the incoming radiation. This effect has a broad area of applications as photodetection, sensing, photovoltaics, etc. Therefore, several techniques have been developed to achieve it in different frequency ranges, such as interference, impedance matching, and design of metamaterials [39].

Among all the kinds of absorbers, ultra-thin films are particularly interesting for applications. The 2D crystals mentioned before have potential in this area because they easily form think slabs. Therefore, Graphene [40] and hBN [41] have been used as absorbers, but their perfect absorption is given from the IR to the microwave regime. Using MoS_2 instead is an option for visible frequencies.

Here perfect absorption of TE polarized light is obtained in few layers of MoS_2 on glass when illuminating at high angles (figure 2.5(a)). MoS_2 high permittivity allows to achieve perfect absorption by breaking the symmetry with a reflector [42]. The reflector is given by the glass substrate at angles above the critical angle, meaning that there is Total Internal Reflection in the glass and no light is transmitted.

Figure 2.5(b-f) shows $R \to 0$ in the reflection spectra in logarithmic color scale at different angles of incidence. The plotted angles are higher than the critical angle and absence of transmission means that the absorption is simply, $A = 1 - R$. By measuring below the light-line, even the monolayers showed an increase of absorption from $< 10\%$ [43] to $\sim 80\%$ around the C exciton (figure 2.5(c)). This is a simpler approach to increase it, in comparison to previous methods [40, 43, 44].

Moreover, the clear variations of perfect absorption regions (angle and frequency in figure 2.5(c-e)) depending on the number of layers could be used to distinguish the number of layers. The perfect absorption of TE polarized light disappears for thicker slabs (> 10 layers) as can be observed in figure 2.5(f). TM polarized light can show perfect absorption for thick slabs (> 50 layers) as will be shown in figure 4.3.

The perfect absorption of light in just a few nm slabs of MoS_2 is an example of tailoring structures with different permittivities to change the optical response of a system.

Summarizing, this section focused on the optical properties of materials via understanding the permittivity of different materials. The concept of "resonance" in the Lorentz model was described and the peaks appearing in the $\mathrm{Im}(\varepsilon)$ were related to the peaks in absorption of the material. The resonances are given by different physical mechanisms, such as vibrational and electronic transitions, or phonons and excitons in crystals. The importance of having different materials with varied permittivities interacting to tailor optical responses was highlighted, and used to achieve perfect absorption in very thin layers. In the next section, optical resonances will be discussed, as well as how to calculate them in simple geometries.

2.2 Optical resonators

Optical resonators confine light [45]. Intuitively, a resonant cavity can be understood as a set of boundary conditions that reflect light back and forth, creating areas in the cavity with enhanced electromagnetic field. There is a broad variety of resonators, dielectric and metallic ones [46, 47]. In fact, the plasmonic nanoparticles discussed before are a very commonly used resonator.

More generally, an optical resonance is the response of an electromagnetic normal mode to incoming light. A normal mode is a stationary solution of the source-less Maxwell's equations in a given closed system. A closed system means that it has

perfect boundary conditions, such that no radiation is leaked to the environment, this implies that the eigenfrequencies associated to such modes are real.

The systems discussed in this thesis do not have perfect boundaries, thus they leak radiation to the environment, and for that they are called *open* systems. This means that their modes decay in time. Thus, the solutions of the open system, source-free, Maxwell's equations are instead called *quasinormal modes* (QNMs) [48, 49]. The eigenfrequencies of the QNMs are complex, $\tilde{\omega}_n = \omega_n - \mathrm{i}\gamma_n/2$, where γ is related to the radiative losses (broadening of the resonance). Intuitively, the smaller γ_n is the longer the photons stay in the resonator. The figure of merit for the "trapping" efficiency of the resonator is the *quality factor*, $Q_n = \omega_n/\gamma_n$ (for the n-th mode) [15, 48].

Here, the optical resonances in dielectrics are described in 3 simple geometries, for which we can find the QNMs analytically: slabs, cylinders and spheres. Depending on the geometry, the QNMs manifest in reflection, transmission or extinction measurements or calculations. They appear as peaks (dips) in extinction cross-sections (reflectivity) measurements, such calculations are also shown here. A detailed description of the calculations of QNMs and reflectivity and cross-sections is given in the Methods section 5.1.

Of course, more geometries sustain optical resonances but they are more challenging to solve and require numerical methods that are beyond the scope of this text. Next, *Fabry-Pérot* cavities are described, which are the most popular resonators.

2.2.1 Fabry-Pérot resonators

A Fabry-Pérot (FP) resonator, also called planar microcavity, is given by two reflecting surfaces. Light bounces between them and constructively interferes generating resonances. Usually the reflecting surfaces are either metallic or Bragg mirrors.

In a FP with perfect conductors as boundaries, the solutions are such that the thickness of the FP cavity, L, determines the resonant wavelength at normal incidence: $\lambda_m = L2n/m$. In this case, $n = \sqrt{\varepsilon}$ is the refractive index between the mirrors and $m = 1, 2, 3, ...$ is the order of the mode. Moreover, at higher angles of incidence ($k_x = k_0 \sin\theta$) the dispersion is parabolic [15]. We will use this information again in Section 3.3.

Reflections to form a FP resonance can also be given in a dielectric slab by total internal reflection, for which the refractive index of the dielectric n has to be larger than the one of the surrounding media. Figure 2.6(a) depicts such example with a dielectric slab with thickness L in vacuum.

Figure 2.6(b) shows the reflectivity calculation (see Methods, equation 5.6) for various angles of incidence, $k_x = k_0 \sin\theta$ of a 200 nm thick slab of $\varepsilon = 2.15$ eV (typical for J-aggregates). Above the light-line (in green) the radiating Fabry-Pérot resonances are visible as dips in the reflectivity.

On top of the reflectivity colormap in figure 2.6(b), the dashed blue lines represent the calculations of the 1st and 2nd FP QNMs eigenfrequencies. Below the light-line the dispersion (ω dependence on k) is different because they are guided modes, the poles are shown as orange dashed lines.

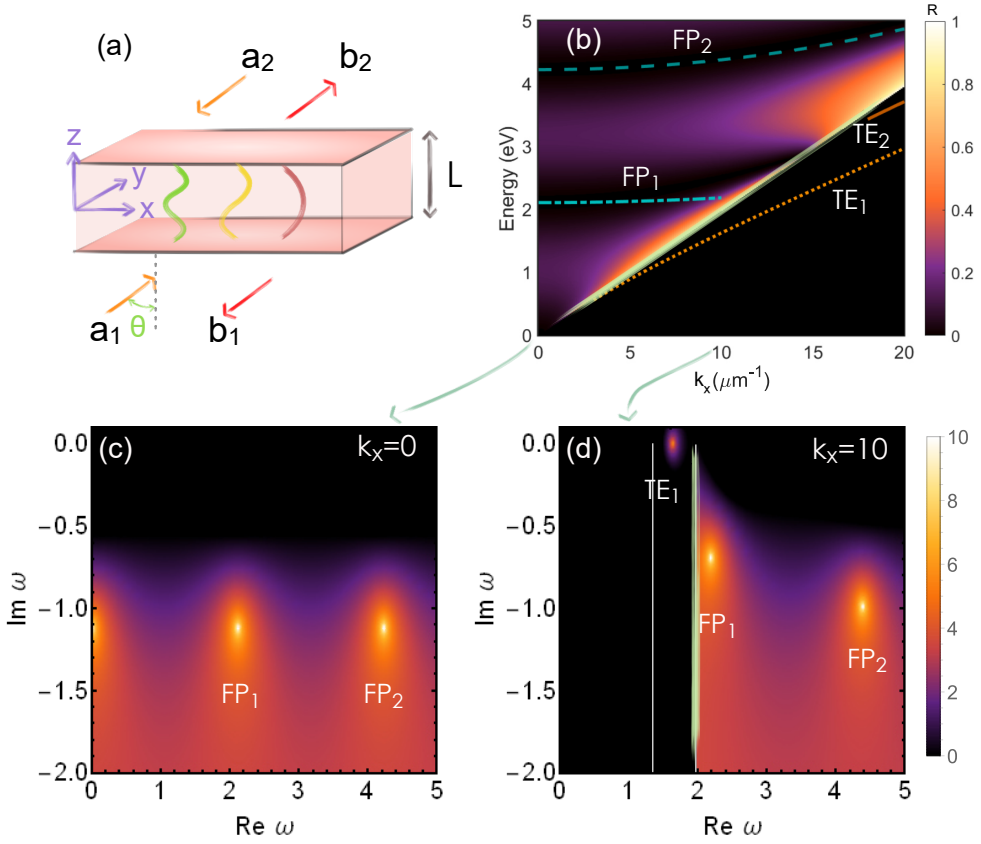

FIGURE 2.6: Fabry-Pérot (FP) étalon with $\varepsilon = 2.15$ and $L = 200$ nm with TE polarized incident light. (a) Schema of the dielectric slab with the FP resonances represented in colors. (b) Reflectivity calculation of the slab, with the QNMs eigenfrequencies in dotted lines. The light-line in vacuum is in light green. (c) FP QNMs frequencies plotted in the complex-ω plane for $k_x = 0\ \mu m^{-1}$. (d) QNMs frequencies for $k_x = 10\ \mu m^{-1}$, below the light-line the guided mode TE_1 is visible and above the light-line the two first FP QNMs.

As mentioned above, the QNMs eigenfrequencies are complex, thus they appear in the complex plane as *poles* of equation 5.6. These poles are visualized in figure 2.6(c) as the highest intensity points. See Methods 5.1 for details on the calculations. The poles position in the complex plane, gives us information about the QNMs' measurable frequency, $\mathrm{Re}(\tilde{\omega}) = \omega$, and their decay rate, $\mathrm{Im}(\tilde{\omega}) = \gamma/2$, which vary for different incident polarization and $k-$vectors.

At normal incidence, $k_x = 0\ \mu m^{-1}$, only radiative FP resonances are excited, the poles are shown in figure 2.6(c). By increasing the in-plane component of the wave vector, k_x, in figure 2.6(d), both FP QNMs and guided modes are excited. As expected, the guided modes are lossless, $\mathrm{TE_n}$, $\mathrm{Im}(\omega) \to 0$. This difference in decay rates matters for coupling between optical resonances and matter, as described in chapter 4.

2.2.2 Resonances in cylinders

Let us consider an infinite cylinder with radius a and $\varepsilon = 3.7$, which is typical for the perovskite $CsPbCl_3$ [50]. Figure 2.7(a) shows the fields for both polarizations TE and TM. In panel 2.7(b), the dispersion for TE polarized light is shown. The details of the calculations are in chapter 5.1, but description of the plot is very similar to the previous section. The QNMs above the light-line (in light green) are

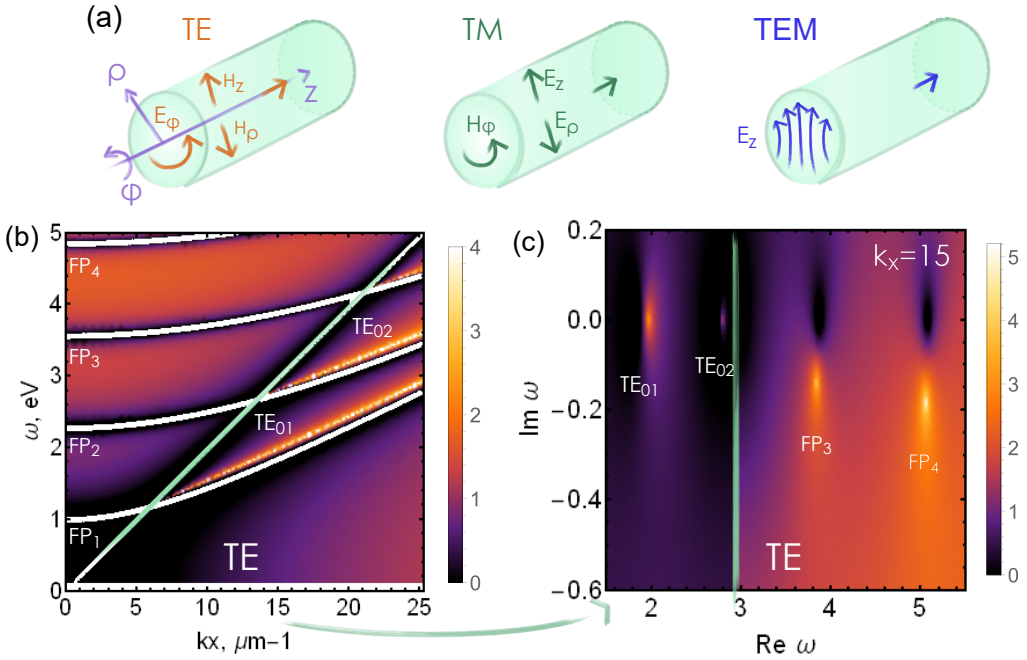

FIGURE 2.7: (a) Schema of fields for TE, TM ($m = 0$) and TEM ($m = 1$, HE11) in an infinite dielectric cylinder in vacuum. (b) Dispersion of the QNMs below and above the light line for a cylinder of radius $a = 250$ nm. (c) Poles (guided and FP) in the complex-ω plane for a $k_z = 15\ \mu m^{-1}$.

FP resonances and the ones below are guided modes. In 2.7(c) the poles are shown for $k_z = 15\ \mu m^{-1}$ where the loss difference is clear, below and above the light-line.

Interestingly, TE has a cut-off even for the lowest mode TE_{01} (azimuthal monopole, $m = 0$ and radial $l = 1$). This means that in 2.7(b), TE_{01} appears only above a critical wave vector, $k > k_c \sim 6\ \mu m^{-1}$. On the other hand the first mode with $m = 1$ (dipole) has no cut-off (TEM). This is a hybrid mode where no clear TE and TM polarizations distinction can be made anymore, so its renamed to HE11 (dipole). The poles are the roots of the characteristic equation 5.10, with $m = 1$ [51]. The dispersion of HE11 is shown in the Supporting Information of the attached publication. We will further discuss the importance of these resonances for strong coupling in the chapter 4.

2.2.3 Mie resonances in spheres

Finally, a water ($\varepsilon = 1.75$) sphere of radius R is considered in vacuum. Gustav Mie made a derivation of a plane wave scattered by a sphere in spherical coordinates in 1908. Such full derivation is clearly explained in [38]. Here, and in the methods section 5.1, the text is limited to describing and using those solutions.

Mie theory describes a plane wave in spherical coordinates (an infinite series of spherical vector harmonics) being scattered. The goal then is to find the coefficients a_l (b_l) that weight the contribution of the l-th spherical harmonic of the TM (TE) mode. Here, a TM (TE) mode is defined as having no radial magnetic (electric) field [38].

The first three radial modes $N = 1, 2, 3$ (computed from equation 5.13) are shown in figure 2.8(c) for the electric dipole, $TM_{1,N}$, of a water sphere of $R = 1.6\ \mu m$. It is clear

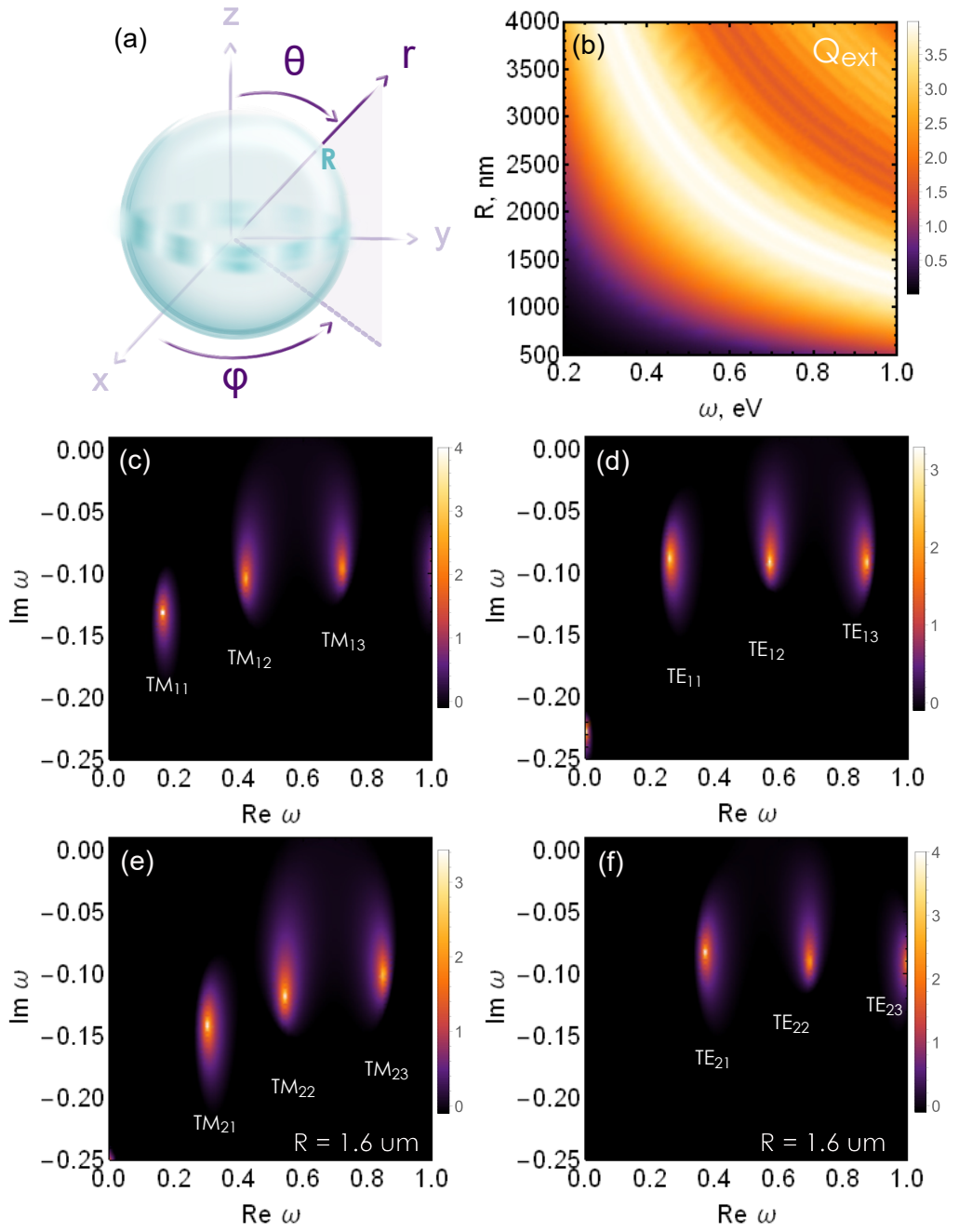

FIGURE 2.8: (a) Schema of spherical coordinates for the water sphere. (b) Extinction efficiency, Q_{ext} for a range of radii. Poles in the complex-ω plane for a sphere of $R = 1.6\ \mu m$ for the coefficients (c) a_1 - electric dipole (d) a_2 - electric quadrupole (e) b_1 - magnetic dipole and (f) b_2 - magnetic quadrupole. All plots show the first 2 radial numbers.

that the losses vary with the radial number N and that the resonance frequencies are different for the magnetic dipole. Moreover, in figures 2.8(e-f) we can see that the energy of the lowest radial mode increases with the orbital number l.

Usually, it is not possible to access each mode experimentally. The most common measurable response of the sphere is the extinction spectra[8]. The extinction and scattering efficiencies are an incoherent sum over all harmonics [38]:

[8]The scattering or absorption can also be measured, where $Q_{ext} = Q_{sca} + Q_{abs}$

$$Q_{ext} = \frac{2}{(k_0 R)^2} \sum_{l=1}^{\infty} (2l+1)\mathrm{Re}(a_l + b_l) \ , \tag{2.10}$$

$$Q_{sca} = \frac{2}{(k_0 R)^2} \sum_{l=1}^{\infty} (2l+1)(|a_l|^2 + |b_l|^2) \ . \tag{2.11}$$

The extinction efficiency for different radii is depicted in figure 2.8(b), where all the resonances are added up into a big resonance which red-shifts with increasing radius and is very broad, in comparison to the broadening given by each γ_n.

This section described the concept of an optical resonance. The typical Fabry-Pérot cavity consisting of two metallic mirrors was described. Then the high refractive index of a material was used as boundary conditions to generate optical resonances. Such optical resonances were described for 3 different geometries. Their QNMs were shown in the complex-ω plane.

In chapter 4, the optical resonances revised here will be strongly coupled to the material resonances described in section 2.1. To get there, next chapter focuses on strong light-matter coupling.

Chapter 3

Traditional Polaritons

In the previous chapter the permittivity of a material was described as the response of materials to an incoming electromagnetic field. The material permittivity was then described as a sum of Lorentzians corresponding to certain types of excitations (electronic or vibrational). Resonant cavities in dielectrics were also shown. Now, the case of trapped light interacting strongly with the material resonance will be considered.

This chapter starts by describing weak, strong and ultrastrong light-matter coupling. For that, there is a short introduction to previous work on strong coupling. Most previous works are widely based on what here are called *traditional* polaritons. These are polaritons formed by an external cavity and a material resonance.

A short quantum mechanical description of strong coupling is given. The main focus is on the Hopfield Hamiltonian, which describes two interacting harmonic oscillators. This is more accurate for the nature of the resonances coupled in this work.

Finally, an example of *traditional* polaritons is discussed: a microcavity coupled to the plasmonic resonance of an array of nanodisks. This system allows to control the coupling strength at room temperature such that it can be tuned from strong to ultrastrong coupling.

3.1 Strong-light matter coupling

The spontaneous emission of light by an atom (or two level system, TLS, in figure 3.1) depends on the available density of photonic states surrounding the atom. Purcell[1] noticed that this meant that the emission rate could be enhanced by locating a cavity close to the emitter (or TLS) to provide it with a high density of photonic states [52]. The Purcell effect has been used to enhance emission rates of molecules around plasmonic nanoparticles for sensing [36]. This effect is part of *weak* light-matter interaction.

Now let us think of a situation when the TLS emits a photon into the cavity, the photon bounces in the cavity for a while, and after some time it is reabsorbed by the atom, only to be emitted into the cavity again and repeat the process. The TLS and the cavity are *strongly coupled* if the electric field in the cavity and the TLS exchange

[1] His work was on relaxation of nuclear magnetic moment transitions, but happened to be more general than that.

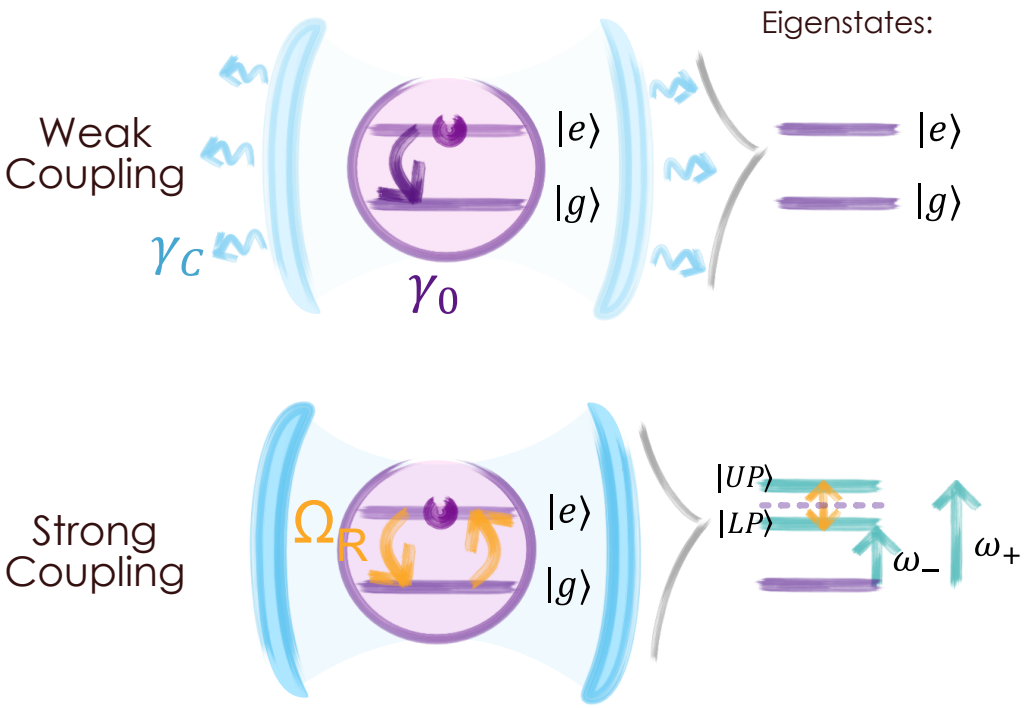

FIGURE 3.1: Weak and strong coupling in the *traditional* configuration with a generic FP cavity, in blue, and a two level system (TLS), in purple. In the weak regime, the losses γ_C and γ_0 are bigger than the interaction between the optical mode and the transition. The eigenstates of the full system are the same as the TLS. In the strong coupling regime, the Ω_R interaction rate is strong enough to split the eigenstates in lower and upper polaritons.

the excitation periodically and the rate at which the atom reabsorbs and emits the photon, Ω_R, is higher than the uncoupled decay rates of the cavity and TLS, γ_c and γ_0, respectively. A schematic of the process is shown in figure 3.1.

Interestingly, when this happens, the eigenstates of the uncoupled TLS and uncoupled photon are no longer solutions of the interacting system. New eigenstates are obtained by diagonalizing the coupled Hamiltonian (e.g., equation 3.4), these are called *polaritons* (upper, $|UP\rangle$, and lower, $|LP\rangle$, polaritons). The new eigenfrequencies $\omega_\pm$ are the resonant frequencies of the polaritons. Thus, the energy levels of the atom are changed by strongly coupling it to light. The change in energy levels is the simplest characterization feature to show strong coupling. For that, the so-called *Rabi splitting* is measured at zero energy detuning of the two components. If the measurement involves several energies of cavity and atom, an anti-crossing feature appears when both energies are tuned (figure 3.2(c-d)).

Strong coupling is a coherent process, which is useful for quantum optical applications. The state of the photons can be shared with the atoms and vice-versa, allowing to write and read superconducting qubits [53]. However, coherence is also interesting for materials composed of several molecules, because when they couple to the same cavity mode they oscillate coherently. This can result in coherent emission from disordered dyes [54]. This effect has demonstrated potential for computational applications in large areas of polariton lattices [55].

By this means, strong coupling has shown capability of tuning matter properties. For example, changing photo-chemical processes [1–3], chemical properties[4, 5], condensation of polaritons [10, 11], charge transport[6], energy transfer[7], and

even empirical work has shown ground state modification[56–59]. A recent review covering most of these developments can be found in [8].

Moreover, the ultrastrong coupling (USC) regime starts when the interaction rate between light and matter becomes comparable to the transition energy, $\eta = \Omega_R/2\omega_0 > 0.1$ [60]. The USC regime requires a Hamiltonian description without approximations, as will be mentioned in the example of microcavity-plasmon polaritons. From such complete description, several interesting phenomena have been predicted by the theory. For example, that the ground state contains virtual photons [61], which can lead to interesting phenomena as dynamical Casimir effect [62, 63].

3.1.1 Traditional polaritons

Several material platforms have been used to achieve strong coupling. Transitions in all kinds of materials (molecules [56], 2DEG intrasubband transitions [64], organic dyes [7], 2D TMDs [65] etc.) have been coupled to various cavities [46, 66]: metallic Fabry-Pérot cavities, dielectric Bragg cavities, photonic crystals, microdisks, etc.

Most of such cavities are closed and the material is hard to reach. Therefore, plasmonic resonances (SPPs and LSPRs) have also been used as nanoresonators to confine light in an open cavity approach and in very small volumes [9], even reaching the single molecule level [67]. Plasmons have been also mixed with all sorts of transitions (organic semiconductors [68], with 2D TMDs [69], quantum dots [70], etc).

All of these platforms have in common that they use one material to provide the transition resonance and a separate structure to form the optical cavity. Here these polaritons are called *traditional polaritons* (see figure 3.1).

However, a different case will be described in the next chapter (4), where polaritons are formed by coupling a photonic mode that is sustained by the same material with a transition resonance (matter part) of the material. These polaritons are denominated here *self-hybridized* or *cavity-free* polaritons.

3.2 Quantum Models

There are several models to understand the strong-light matter interaction: fully classical [71], semi-classical and fully quantum mechanical [9, 60]. To understand the basics of the quantum mechanical models, let us consider one photon in a cavity with field $E = \mathcal{E}(\hat{a}^\dagger + \hat{a})^2$. The photon interacts with a two level emitter (it can only be in the ground, $|g\rangle$, or excited state, $|e\rangle$) with transition dipole moment $\hat{\mu} = \vec{\mu}(\hat{\sigma}^\dagger + \hat{\sigma})^2$ (figure 3.1). This results in the so-called Jaynes-Cummings (JC) Hamiltonian [72],

$$\hat{H} = \frac{\hbar\omega_0}{2}\hat{\sigma}_z + \hbar\omega_c\hat{a}^\dagger\hat{a} + \hbar g(\hat{a}^\dagger\hat{\sigma} + \hat{\sigma}^\dagger\hat{a}) \, . \tag{3.1}$$

The first term corresponds to the free atomic Hamiltonian and $\hbar\omega_0 = E_e - E_g$ is the transition energy[2]. The second term is the electric field Hamiltonian with resonance at $\hbar\omega_c$. The third term is the interaction that creates an atomic excitation while annihilating a photon or vice-versa.

In absence of a driving field, the emitter couples to the vacuum. The coupling strength is given by $\hbar g = \vec{\mu} \cdot \vec{\mathcal{E}}_{vac}$. The vacuum field is $\mathcal{E}_{vac} = \sqrt{\hbar\omega_c/2\varepsilon_\infty\varepsilon_0 V}$, for a mode volume, V. Two important things here are pointed out:

1. The coupling strength is maximized when the transition dipole moment and the field are aligned.
2. The vacuum field, $\mathcal{E}_{vac}$, has a dependence on the cavity resonance that should be considered in the coupling strength when fitting data in the usual anticrossing measurements ($g \propto \sqrt{\hbar\omega_c}$), as shown in figure 3.2(c-d).

This very simple picture works for the original experiments by Haroche, where the interaction was between a single photon and a single Rydberg atom [73], and for experiments of single photons with superconducting Qubits [74]. However, it is not accurate for many of the examples we described in the previous section. There are several extensions of this simple model to include fast rotating terms, several emitters, etc. A good summary on which model is more accurate for each situation can be found in [60, 75].

Research on quantum models is still on going to understand the strong coupling related effects [76–78]. experimentally showed above

3.2.1 Hopfield Hamiltonian

The previously described JC Hamiltonian explores the interaction between a fermionic and a bosonic field. A description of the interaction of two bosonic fields is needed here because here two macroscopic oscillators are considered: i) an optical resonance ii) a transition resonance of a material (phonon, exciton, vibrational,...) or a plasmonic resonance.

Such Hamiltonian was developed by Hopfield to better understand excitons in crystals [12] and reads as follows,

$$\hat{H} = \hbar\omega_0 \hat{b}^\dagger \hat{b} + \hbar\omega_c \hat{a}^\dagger \hat{a} + \hbar g(\hat{a}^\dagger + \hat{a})(\hat{b}^\dagger + \hat{b}) + \frac{\hbar g^2}{\omega_0}(\hat{a}^\dagger + \hat{a})^2 \,, \tag{3.2}$$

where the first two terms represent the uncoupled oscillators. The third term is the interaction term of both fields with $g = \mu\sqrt{\rho V}\mathcal{E}_{vac}\omega_0/\omega_c$, in the Coulomb gauge[3]. Finally the forth term is the diamagnetic term (or A^2 term), which becomes important when the coupling strength is large enough ($g/\omega_0 > 0.1$). Interesting phenomena predicted for USC and beyond arise from this term [81]. The eigenvalues of this lossless Hamiltonian are the following [80],

$$\omega_\pm = \frac{\sqrt{\omega_c^2 + 4g^2\omega_c/\omega_0 + \omega_0^2 \pm \sqrt{(\omega_c^2 + 4g^2\omega_c/\omega_0 + \omega_0^2)^2 - 4\omega_c^2\omega_0^2}}}{\sqrt{2}}, \tag{3.3}$$

[2] $\hat{\sigma} = |e\rangle\langle g|$ and $\hat{\sigma}^\dagger = |g\rangle\langle e|$ are the atomic transition operators and $\hat{\sigma}_z = [\hat{\sigma}, \hat{\sigma}^\dagger]$.

[3] The gauge choice does not change the values of the observables, thus one could use the dipole gauge and obtain the same eigenvalues [79, 80].

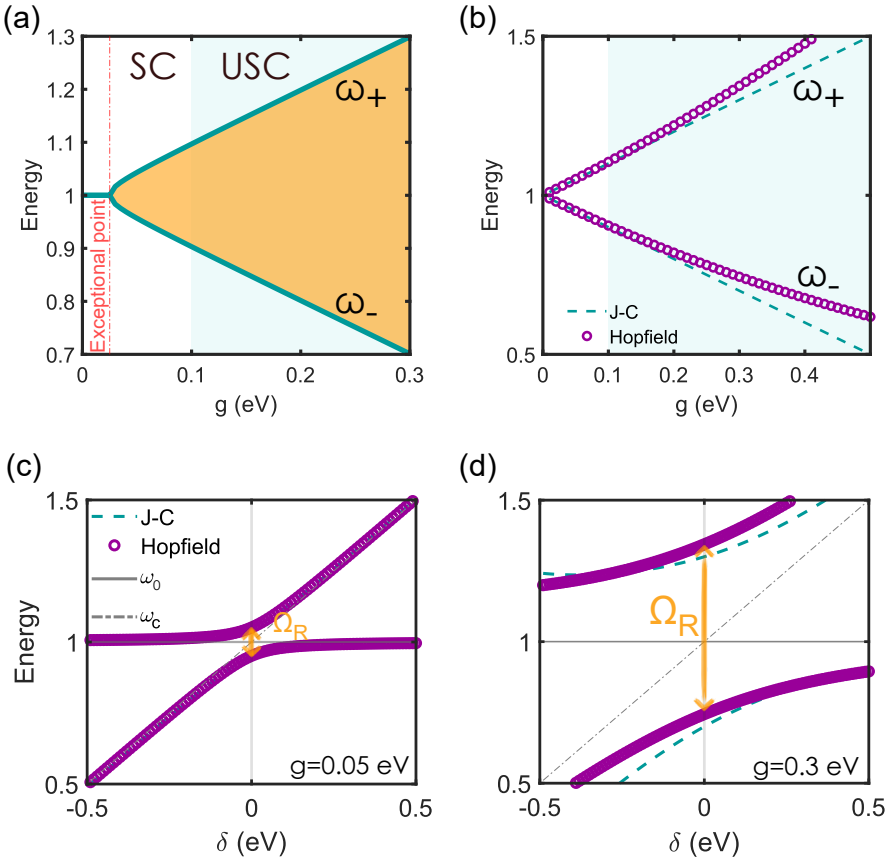

FIGURE 3.2: Top: (a) Eigenvalues of Jaynes-Cummings (JC) with loss with $\omega_0 = \omega_c = 1$ eV for different coupling strengths. After the exceptional point (red dotted line) the polaritons separated by Rabi splitting, in orange, are visible. (b) Comparison between eigenvalues of lossless JC and full Hopfield Hamiltonian for various values of g. Bottom: Anti-crossing calculations for Hopfield and JC Hamiltonians, by varying $\delta = \omega_0 - \omega_c$, for different coupling strengths (c) $g = 0.05$ eV, in the SC regime, and (d) $g = 0.3$ eV, in the USC regime.

The terms corresponding to the JC Hamiltonian (equation 3.1) can be obtained from Hopfield Hamiltonian (equation 3.2), by using two approximations: the Rotating Wave Approximation (RWA)[4] and neglecting the diamagnetic term[5]. Under this simple approximations it is also possible to add losses as [46],

$$\hat{H} = \hbar \begin{pmatrix} \omega_0 - \mathrm{i}\gamma_0/2 & g \\ g & \omega_c - \mathrm{i}\gamma_c/2 \end{pmatrix} , \tag{3.4}$$

where the eigenvalues are,

$$\tilde{\omega}_\pm = \frac{\omega_0 + \omega_c}{2} - \mathrm{i}\frac{\gamma_0 + \gamma_c}{4} \pm \sqrt{g^2 - \frac{(2\mathrm{i}\delta - (\gamma_c - \gamma_0))^2}{16}} . \tag{3.5}$$

Here, $\delta = \omega_0 - \omega_c$, is the detuning. In the resonant case, $\delta = 0$, $\Omega_R = \omega_+ - \omega_- = \sqrt{16g^2 - (\gamma_0 - \gamma_c)^2}$. Ω_R has real values for $4g > |\gamma_0 - \gamma_c|$ and, in such case, it is

[4] In this case the counter rotating terms $\hat{a}\hat{\sigma}$ and $\hat{a}^\dagger\hat{\sigma}^\dagger$ are negligible because they annihilate or create a photon and an excitation in the atom simultaneously. Thus, they do not preserve energy unless there are several transitions to be excited and/or several photons [72].

[5] Assuming that g is small, then $g^2 \to 0$.

called Rabi splitting[6]. This is depicted in figure 3.2(a), where the red line marks the exceptional point, $4g = |\gamma_0 - \gamma_c|$[7]. After this point the coupling strength overcomes the losses and the two polaritonic branches emerge. To experimentally resolve the two polaritons, the splitting should be larger than the uncoupled line widths, $\Omega_R > (\gamma_0 + \gamma_c)/2$.

These approximations are commonly used for SC cases, but sometimes the full Hamiltonian is necessary. To see when the approximations are valid in the lossless case, figure 3.2(b) compares the solutions between the JC approximations and the full Hopfield Hamiltonian. For low values of g (white background), both have the same solutions. However, they considerably differ in after $\eta = g/\omega_0 > 0.1$ (shadowed in blue). In that region, the full Hopfield eigenvalues (purple circles) do not increase linearly with respect to the coupling strength. This is the main signature of USC regime.

The anticrossing plot in figure 3.2(c) shows that the eigenvalues of both are identical for small values of g even at large detuning. Nevertheless, for $g = 0.3$ eV, variations are noticeable even at $\delta = 0$, see figure 3.2(d). In the following section a plasmon-microcavity platform with flexibility to achieve both SC and USC is described. Therefore the full Hopfield description will be necessary for an accurate description.

3.3 Plasmons and microcavities polaritons

To increase the coupling strength one can either increase the dipole moment of the transition, $\vec{\mu}$, or decrease the mode volume of the cavity, V. However, very often ω_0 and $\vec{\mu}$, are inherent from the material. Thus, the common approach is to build the cavity to control the mode volume by decreasing it as much as possible (the community pushed this limit with plasmonic resonators [67]) and to tune the cavity frequency, ω_c, to reach zero detuning, $\delta = 0$, for measuring the Rabi splitting.

Coupling plasmonic nanoparticles with microcavities provides freedom to tune the detuning, δ and coupling strength, g, at room temperature [80, 82]. This freedom is given by tuning the parameters depicted in figure 3.3. Previously such microcavity-plasmon polaritons has been used to increase the splitting with excitonic materials [82] and to achieve ultrastrong coupling at room temperature and without magnetic fields [80].

To form polaritons with different coupling strengths, different arrays of gold nanodisks were fabricated in between two gold mirrors separated by a thickness L, as depicted in figure 3.3(a). This cavity thickness determines the frequency of the optical resonance, ω_c, which increases with the angle of incidence in a parabolic manner. The arrays of nanodisks are all 20 nm in height but vary in diameter, $d = 60, 80$ and 100 nm, and pitch between disks, $\Lambda = 100, 140, 180, 220, 260, 300$ and 340 nm (figure 3.3(b)). See the methods section (5.2.1) for details on the fabrication methods.

The polaritons were optically measured by normal incidence and angle resolved spectroscopy as detailed in section 5.3.1. In the reflection measurements, the polaritons appear as pronounced dips (figure 3.3(c-e)).

[6] Through this text and appended paper *Rabi splitting* is found at $\delta = 0$.

[7] This means that we can reach strong coupling by matching the losses of the cavity and the emitter.

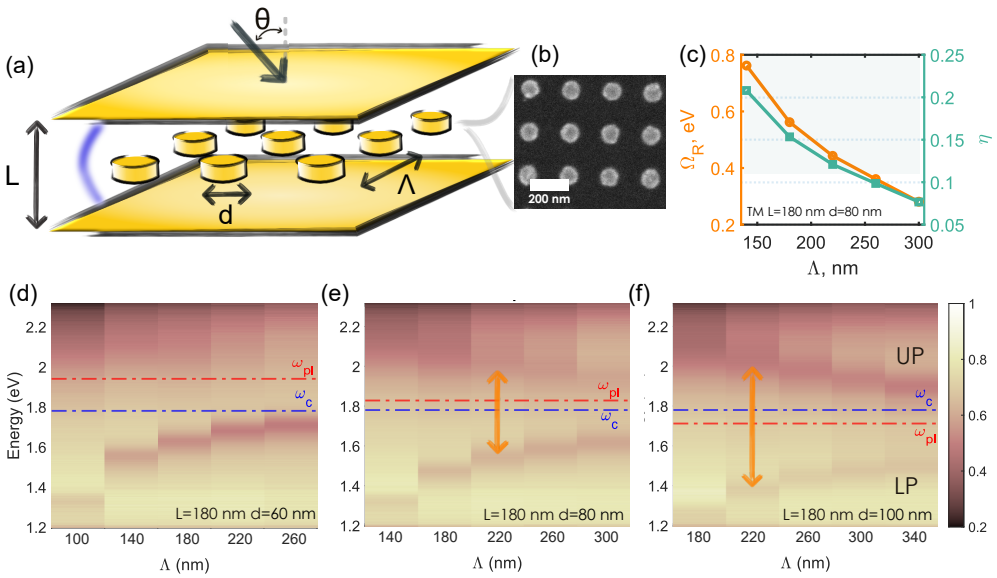

FIGURE 3.3: (a) Schema of the disks (20 nm height) between the FP mirrors (30 nm thick). The varied parameters are labeled: L - distance between mirrors, d - diameter of disks, Λ - center-to-center distance between particles, θ - angle of incidence. (b) SEM of the disk array for $d = 80$ and $\Lambda = 200$ nm. (c) Values of Ω_R and η for TM polarization at zero detuning with $L = 180$, $d = 80$ nm, the USC region is shaded in blue. Reflection at normal incidence measurements of the polaritons formed for a cavity with $L = 180$ nm with varying pitch, Λ, and (d) $d = 60$ nm (e) $d = 80$ nm and (f) $d = 100$ nm. The Rabi splitting is marked in orange.

For a fixed cavity, ω_c, the detuning is controlled by the diameter of the nanodisk, which determines the resonance of the plasmon ω_{pl}. The smaller the diameter the higher the resonance energy. In figure 3.3(d-f) we can see the the energy of the plasmon in red dotted lines. For panel (e) the detuning is almost zero and we can see that both polaritonic branches are almost equally dark in the color plot of reflection. This is because at zero detuning the loss of both polaritons is the same, since they are half photonic and half plasmonic. When the detuning increases as in panel (f), the upper polariton (UP) is closer to the uncoupled cavity, ω_c, and it is darker because the cavity transmits light at that frequency. The lower polariton (LP) is closer to the plasmon, ω_{pl}, and thus it reflects more light. The opposite case is found for panel (d), where the LP is more photonic and the UP is more plasmonic. In this case, the UP in (d) is almost invisible because of the interband transitions in Au (see figure 2.4(a)). This is an empirical description, but the "amount" of photon and plasmon of each polariton can be quantified by the Hopfield coefficients [12]. This will be quantified in the future to show the correlation.

Moreover, the size of the disk does not only control the detuning by determining ω_{pl}, it also determines the dipole moment[8], μ_{pl} [82]. Bigger disks have a larger dipole moment (as seen in the extinction intensity in figure 2.4(c)) and thus larger coupling strength g. This is clear by comparing nanodisks diameters with a fixed $\Lambda = 200$ nm, the orange arrow in figure 3.3(d), $d = 80$ nm, is larger than the one in 3.3(e) $d = 100$ nm.

In fact, $g = \mu_{pl}\sqrt{a^2\rho}\mathcal{E}_{vac}\frac{\omega_{pl}}{\omega_c}$, where $\mathcal{E}_{vac} = \sqrt{\frac{\hbar\omega_c}{2\varepsilon\varepsilon_0 L_{eff}a^2}}$ per unit area, a^2. The density of nanodisks depends of the pitch as, $\rho = 1/\Lambda^2$. The effective cavity length is $L_{eff} =$

[8]Here only the in-plane dipole moment is considered, which varies with the diameter of the disk and not the out-of-plane one, since the height is fixed.

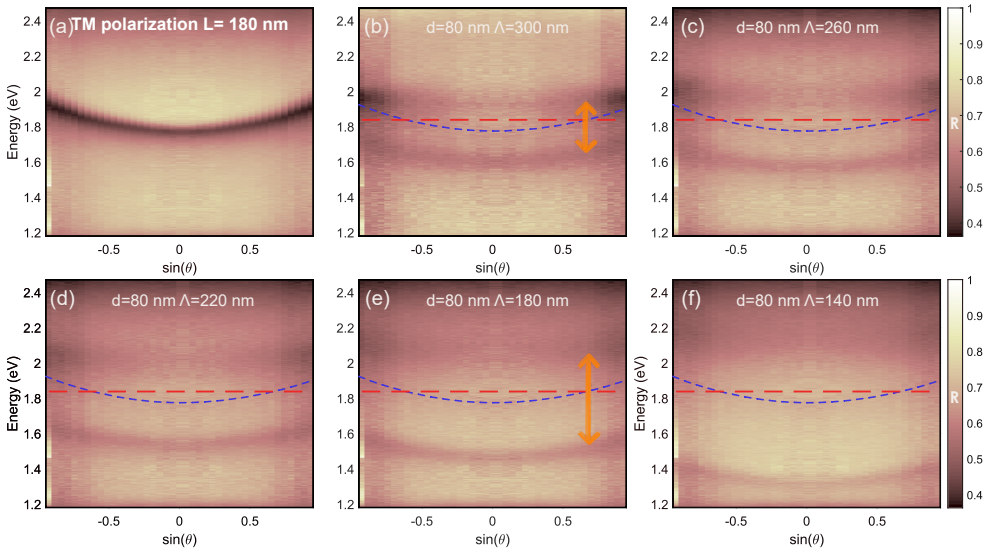

FIGURE 3.4: Dispersion of polaritons for TM polarized light. $L = 180$ nm and $d = 80$ nm. The red dashed line shows the peak of the uncoupled plasmon and the blue dashed line the empty cavity dispersion showed in (a). Dispersion in reflection of arrays with different pitches varies the coupling strength, resulting in polaritons from SC to USC regime: (b) $\Lambda = 300$ nm, $\Omega_R \approx 0.28$ eV, (c) $\Lambda = 260$ nm, $\Omega_R \approx 0.36$ eV, (d) $\Lambda = 220$ nm, $\Omega_R \approx 0.44$ eV, (e) $\Lambda = 180$ nm, $\Omega_R \approx 0.56$ eV, (f) $\Lambda = 140$ nm, $\Omega_R \approx 0.76$ eV.

$\lambda/4n = \frac{hc}{4n\hbar\omega_c}$ [83]. Thus, the coupling strength is expressed as,

$$g = \frac{\mu_{pl}}{\Lambda}\sqrt{\frac{\hbar\omega_c}{2\varepsilon_0\varepsilon L_{eff}}}\frac{\omega_{pl}}{\omega_c}\,. \tag{3.6}$$

Then the coupling strength is higher for large d and small Λ. This explains the behaviour of each panel in figure 3.3(d-f), where the Rabi splitting (distance between dips) increases for smaller values of Λ.

All the previous observations were done for normal incidence, where ω_c is fixed by L. It is also possible to fix ω_{pl} and vary ω_c by using its angular dependence. Chapter 2.2 mentioned that FP cavities have parabolic dispersion in energy, which is observed in 3.4(a) and 3.5(a), and it is clear that the dispersion depends on the polarization.

Dispersion allows to obtain $\delta = 0$ for $\theta \neq 0$. In figure 3.4 $\delta = 0$ for $\sin\theta = 0.63$. By extracting the energy difference of the polaritons at that angle, it is possible to plot the Rabi splitting dependence on Λ as showed in figure 3.3(c). Ideally, the measurements in figure 3.3 would be the same as $\sin\theta = 0$ in figure 3.4, but measurements at normal incidence are in reality the sum of several small angles up to $\sin\theta = 0.4$, due to the finite numerical aperture of the collecting objective (see Methods). Thus, finding the point of zero detuning in dispersion is more precise to obtain the Rabi splitting.

In figure 3.4, a gap is visible between the two polaritons and it increases from panel (b) to (f). This is the polaritonic gap, it increases with the coupling strength and is a signature of the USC regime. Further analysis on the behavior of the polaritons for different θ is involved in TM polarization because the **E**-field is not always parallel

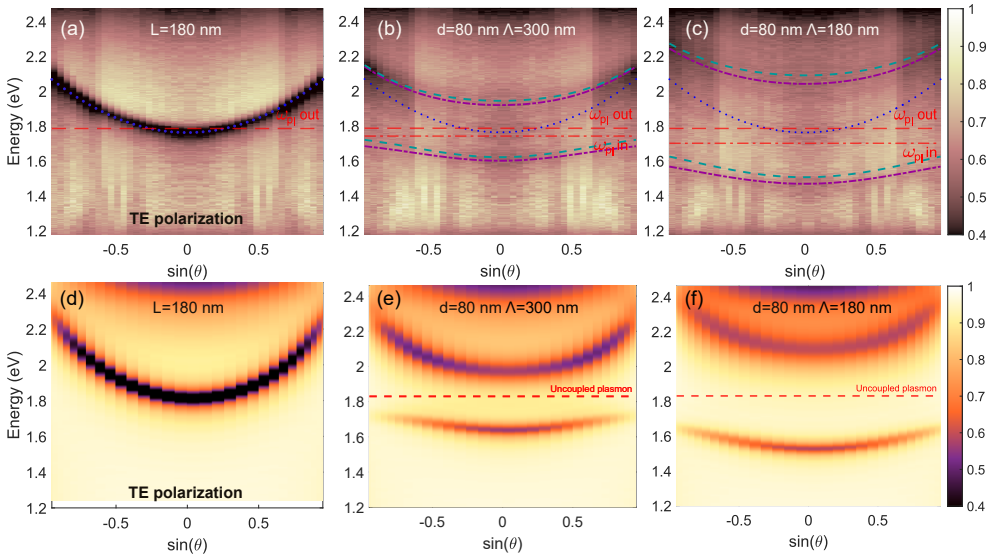

FIGURE 3.5: Top row measured dispersion in reflection of $L = 180$ nm and $d = 80$ nm in TE polarization. (a) Empty cavity. Measured dispersion of $d = 80$ nm with solutions to the Hopfield Hamiltonian (b) $\Lambda = 300$ nm and (c) $\Lambda = 300$ nm.

to the long axis of the disks. Meaning that the in-plane μ_{pl} is not aligned to $\mathbf{E}_{\mathrm{TM}}$, then $g(\theta)$ varies accordingly.

TE polarization simplifies the picture (see figure 3.5) because the coupling strength depends only on the detuning $g(\theta) \propto \frac{\omega_{pl}}{\omega_c}$, because $E \parallel \mu_{pl}$. The top row in figure 3.5 shows the measured dispersion for the empty cavity with $L = 180$ nm and for disk arrays of $d = 80$ nm for $\Lambda = 300$ and 180 nm.

The Hopfield Hamiltonian (equation 3.2) can be used here to find the energy of the polaritons. The blue dashed lines in 3.5(b) and 3.5(c) are the Hopfield eigenenergies for $g_{\Lambda=300} = \Omega_R/2 = 0.16$ eV and $g_{\Lambda=180} = 0.29$ eV at $\delta = 0$, where $\omega_{pl} = 1.785$ eV is the maximum of the plasmon in free space (as measured outside of the cavity, and showed in a red dashed line). It is interesting to see that the Hopfield eigenenergies almost reproduce the polaritonic dip in reflection. Nevertheless, if we assume $\omega_{pl,\Lambda=300} = 1.74$ eV (red dot-dash line), the solutions (in purple dot-dashed lines) seem to reproduce the experimental polaritons. Moreover, when decreasing the pitch of the array, to match the experimental polaritons we need to assume an even lower frequency, $\omega_{pl,\Lambda=180} = 1.71$ eV, for the eigenvalues to match the experimental dips. Of course, this observation requires rigorous statistical analysis, which will be done in the future, in both experimental and simulated data (as shown in figure 3.5(d-f)).

Nonetheless, let us expand on the interest behind this observation. Huppert et al., showed that USC with free-radiation is obtained when the matter resonance has a very large oscillator strength and the radiative broadening is of the same order of magnitude as the resonance frequency ω_0 [84], as is the case for metallic nanodisks. This would mean that the plasmonic response in free-space can be perceived as the plasmonic array ultrastrongly coupled to free-space modes. Inside the cavity, the plasmonic array is not in USC with the free-radiation and thus the ω_{pl} is not "dressed" anymore by the continuum of the free-space modes, explaining the shift of the plasmon inside the cavity. Future experiments and simulations are needed to

clarify the effect of nanoparticle size, d, and pitch of the array, Λ, on the mismatch between the plasmon resonance inside and outside of the cavity.

This would mean that the array of nanodisks can achieve SC without the need of a cavity by coupling to free-space. The need of an external cavity will be questioned once more in the following Chapter.

Chapter 4

Cavity-free polaritons

The previous chapter discussed *traditional* polaritons created by an external cavity mode. This Chapter will explore the *self-hybridized* polaritons, where no external cavity is needed anymore. This chapter is closely related to the appended paper [85], but some additional material, and comments on recent exciting developments from the community, are included.

First, a description of *Bulk polaritons* is given for Lorentz materials. Then, a discussion on coupling various optical modes (strictly speaking they are QNMs[1], but for simplicity will be called modes throughout the Chapter) in the reshaped material as described in Chapter 2.2.

The first studied geometry is dielectric slabs, where the existence of polaritons is shown in J-aggregates, hBN and MoS_2. This is followed by a discussion on perovskite cylinders. In both examples polaritonic states are shown above (coupling to FP modes) and below (coupling to guided modes) the light-line. Finally, vibrational polaritons are discussed, which naturally occur in micrometer-sized water spheres.

The chapter is closed by discussing the limit of the Rabi splitting in *self-hybridized* Lorentz materials and the limits of the structure dimensions to form polaritons.

4.1 Bulk polaritons

An important point to highlight is that Hopfield's work describes the interaction of a plane wave with a bulk crystal [12]. As shown in the appended paper [85], the Bulk polariton modes are found as roots of the dispersion equation of a plane wave in a Lorentz material,

$$kc - \omega\sqrt{\varepsilon(\omega)} = 0 \ , \tag{4.1}$$

where $\varepsilon(\omega)$ is given by a simple Lorentz formula (equation 2.5). Hence, the coupling strength can be expressed in terms of the oscillator strength f (equation 2.6) and plasma frequency ω_P of the Lorentz medium as $g = (\omega_P/2)\sqrt{f\omega_0/\varepsilon_\infty\omega_c}$. Thus, the coupling strength of bulk polaritons depends only on the material.

The vacuum Rabi splitting is then obtained as the difference between the two polariton energies of the Hopfield lossless Hamiltonian (equation 3.3) for

[1] As mentioned in Section 2.2, since the system is open, the modes here are *quasinormal modes* (QNMs). A description is given in the Methods section 5.1

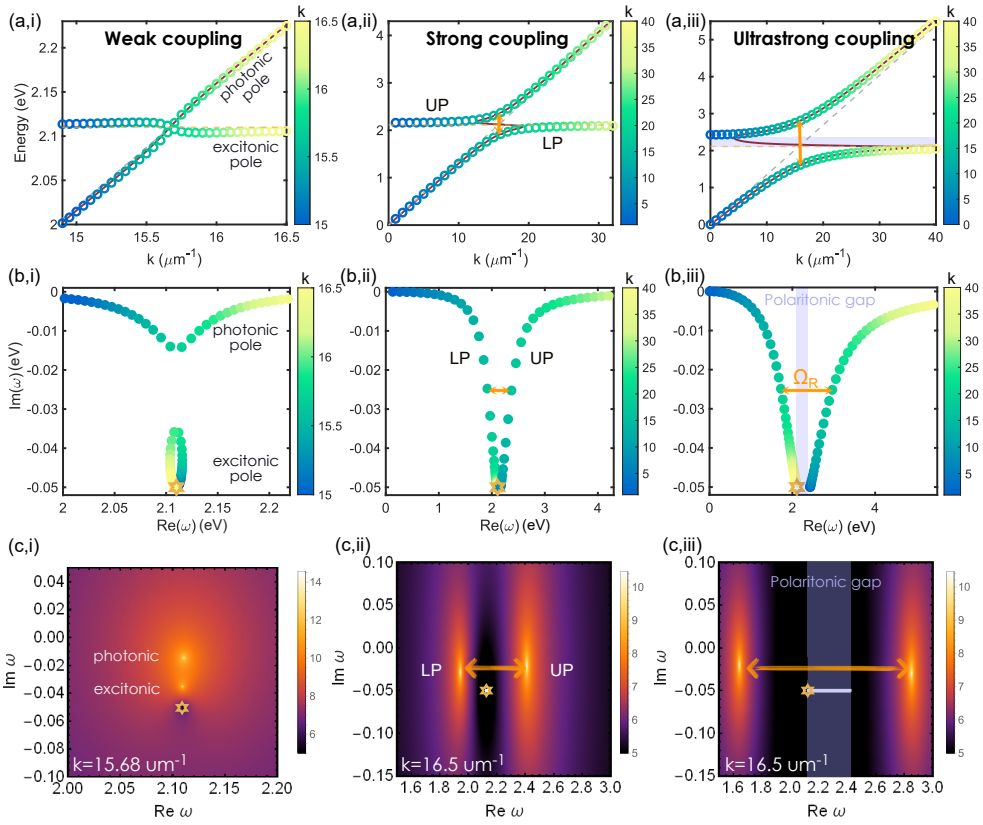

FIGURE 4.1: Bulk polaritons of J-aggregates with different oscillator strengths. The first column (i) shows the weakly coupled case: $f\omega_P^2 = 0.0045\ eV^2 < \varepsilon_\infty\gamma^2/4$. The second column (ii) shows the strongly coupled case: $f\omega_P^2 = 0.445\ eV^2 > \varepsilon_\infty\gamma^2/4$. The third (iii) column shows the USC case: $f\omega_P^2 = 3.116\ eV^2$ and $g_0/\omega_c \sim 0.29$. The different rows present the modes differently, the first row (a) shows the usual dispersion: $\mathrm{Re}(\tilde{\omega}_c)$ vs k. The second row (b) shows the trajectories of the modes in the $\tilde{\omega}$-plane. The third row (c) shows the modes for specific k-vectors corresponding to $\delta = 0$ in each case. The position of the uncoupled exciton $\omega_0 - i\gamma/2$ is marked with a star and the polaritonic gap is shaded in blue. Figure modified from [85].

$\delta = \omega_0 - \omega_c = 0$:

$$\Omega_R = \sqrt{2g^2 + \omega_0^2 + 2g\sqrt{g^2+\omega_0^2}} - \sqrt{2g^2 + \omega_0^2 - 2g\sqrt{g^2+\omega_0^2}} = 2g_0\ , \tag{4.2}$$

where $g_0 = (\omega_P/2)\sqrt{f/\varepsilon_\infty}$ is the zero-detuning coupling strength. Here $2g_0$ is referred to as the *bulk Rabi splitting* of the material.

The Hopfield model does not include losses, but an extension by Huttner and Barnett [86] found that polaritons appear if:

$$f\omega_P^2 > \varepsilon_\infty\gamma^2/4\ . \tag{4.3}$$

This can be rewritten as $g_0 > \gamma/4$, which is the usual strong coupling criterion mentioned before, but with a lossless cavity, $\gamma_c = 0$ [61, 86]. The modes were calculated in the $\tilde{\omega}$-plane (see Methods 5.1), to obtain the real frequency and decay rate (imaginary component) of the polaritons.

The roots of equation 4.1 are shown in figure 4.1 for J-aggregates [21]. J-aggregates are interesting because the exciton oscillator strength can decrease by diluting them. Thus in figure 4.1 different oscillator strengths of J-aggregates are shown, resulting

in weak, strong and ultrastrong coupling in the bulk. The permittivity for the SC case was shown in figure 2.1.

The modes are found for each wave vector, k, and the results are shown in different formats. The first row (b) in figure 4.1 shows the usual dispersion plots for the 3 regimes, to show the typical anticrossing in SC and USC regime. The 2nd row (b) shows the trajectories of the modes in the $\tilde{\omega}-$plane, where the color scale gives information on the wave vector corresponding to each pair of poles. These trajectories are extracted from finding the poles in the complex plane for different wave vectors. Examples of this complex plane color plots are shown in figure 4.1(c,i-iii), for k at zero detuning, $\delta = 0$. In these plots the modes are the points with higher intensity. In the case of weak coupling, 4.1(c,i), the poles corresponding to the photon (top) and the exciton (bottom) are degenerate in the real frequency, meaning that they cross in the dispersion plot in 4.1(a,i). It is interesting to see that while the loss, $\mathrm{Im}(\tilde{\omega})$, in the excitonic pole decreases (the uncoupled exciton is showed as a yellow star), it increases in the photonic pole (figure 4.1(b,i)). Even though there is no anticrossing, the presence of the excitonic resonance affects the plane wave and vice-versa. This corresponds to the weak coupling regime, also know as the Purcell effect [52].

In the 2nd (ii) and 3rd (iii) column of figure 4.1 shows the Rabi splitting (orange arrow) appearing at zero detuning, then the degeneracy discussed above is broken. This splitting is observed in the dispersion plot as the characteristic anticrossing in 4.1(a,ii) and 4.1(a,iii) respectively. In the trajectories 4.1(b,ii) and 4.1(b,iii), the LP starts, $k = 0\ \mu m^{-1}$, being mainly photonic and ends, $k = 40\ \mu m^{-1}$, being mainly excitonic. At the point of the Rabi splitting ($\delta = 0$) each polariton has an imaginary part of $\gamma/4$. These cases correspond to the strong coupling regime in (ii) and USC in (iii). Moreover, for the USC case the polaritonic gap ($\Delta_{pol} = \sqrt{\omega_0^2 + 4g_0^2} - \omega_0$ [85]) is visible and shaded in blue.

In this section, the existing electromagnetic modes in a bulk of a Lorentz material were discussed. In particular, when the material fulfills the condition $f\omega_P^2 > \varepsilon_\infty \gamma^2/4$, the modes are polaritons. In the following sections, the dispersion and trajectory plots will be shown for different geometries, by reducing the dimensions. In such case, the photonic resonances discussed in section 2.2 can couple to the excitations.

4.2 Self-hybridized polaritons in different geometries

4.2.1 2D polaritons in infinite slabs

Now, let us consider an infinite slab in two dimensions (x-y) and confined in z. The slab sustains the optical (FP and guided) resonances discussed in section 2.2. In the appended paper [85], their interaction with the excitonic resonance in J-aggregates [21] was studied. Two different oscillator strengths, mentioned in figure 4.1, were considered. Additionally, the interaction of TE polarized light with an hBN slab, figure 2.3, of 1.75 μm thickness also showed polaritons.

Both slabs J-aggregates and hBN self-couple to both guided and FP modes. Depending on the oscillator strength the interaction can be weak, strong or ultrastrong (USC). Even more so, slabs of J-aggregates with high oscillator strength

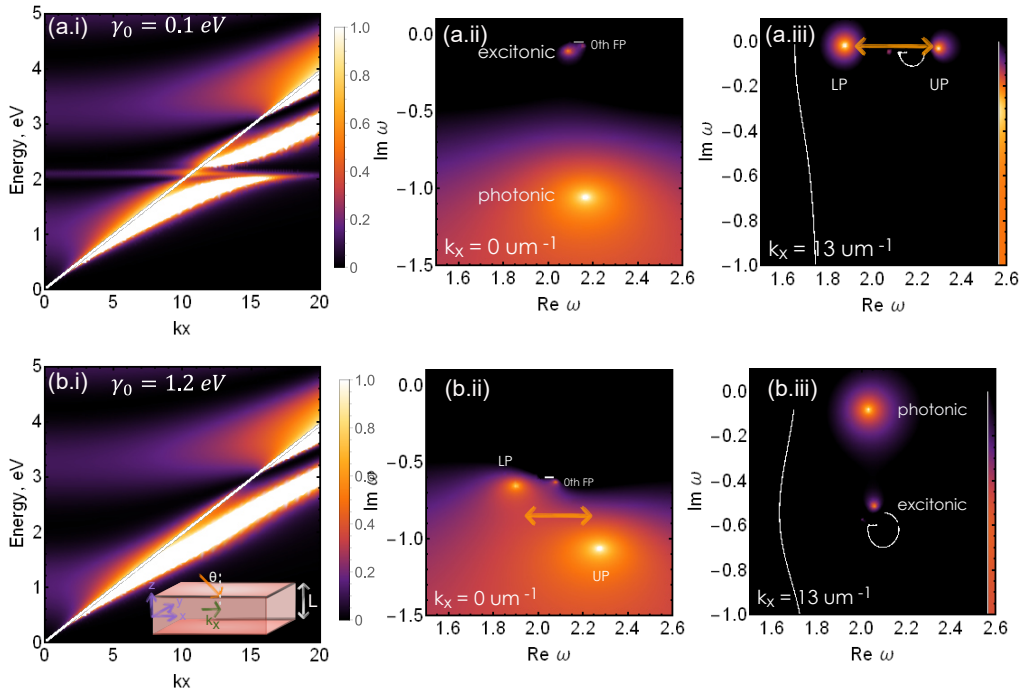

FIGURE 4.2: (i) Reflectivity calculations for TE polarization and modes at $\delta \sim 0$ (ii) above the light-line (iii) below the light-line of a 220 nm thick slab of J-aggregates with $f\omega_P^2 = 0.45\ eV^2$ and (a) $\gamma_0 = 0.1$ eV (b) $\gamma_0 = 1.2$ eV.

and hBN are in the USC regime. J-aggregates with low oscillator strength, $f\omega_P^2 = 0.445\ eV^2$, can be strongly coupled to the slab, but only below the light-line.

It is important to stress that the same excitation can couple differently to each of those photonic modes depending on the photonic losses, γ_c. For example, above the light-line the interaction is such that $|\gamma_c - \gamma_0|/2 \sim 0.5\ eV > 2g_0 = 0.445$ eV, meaning that FP modes are weakly coupled to the exciton[2]. This is shown in figure 4.2(a.ii), where at $\delta \sim 0$ the poles are degenerated in $Re(\omega)$. While below the light-line (figure 4.2(a.iii)), at $k_x = 13\ \mu m^{-1}$, such that $\delta \sim 0$ there are clearly two polaritonic QNMs separated by $\Omega_R \sim 0.42$ eV. In summary, in the top row in figure 4.2, the system is weakly coupled above the light-line and strongly coupled below it.

However, one could imagine the inverse case, where $|\gamma_c - \gamma_0| \sim 0$ for the FP QNMs, but not for the guided modes. In the hypothetical case of $\gamma_0 = 1.2$ eV (bottom row in figure 4.2) two polaritonic modes appear above the light-line, at $k_x = 0$, but the two modes are degenerate (weakly coupled) below the light-line, $k_x = 13\ \mu m^{-1}$. Thus, one should carefully choose the optical mode to couple to specific excitations. In this case, $(\gamma_c + \gamma_0)/2 > \Omega_R$, and therefore the splitting is not visible in reflection, see panel 4.2(b.i).

From the previous paragraph, it is clear that the choice of optical mode to achieve SC depends on the excitation decay rate, γ_0. For some materials, both FP and guided modes can be strongly coupled (even reaching USC regime) at the same time, as in J-aggregates with high oscillator strength and hBN slabs (see appended paper [85]). Most of the excitations used by the community have decay rates of $\gamma_0 < 0.3$ eV [66].

[2]Even though the modes are not splitting, it is possible to see two dips in the reflectivity measurements. There is a variety of optical phenomena, which can lead to such a behavior, including enhanced-absorption, Fano resonances, and electromagnetically induced transparency [87]

Thus, for usual materials, in the case of self-hybridized polaritons, the coupling is stronger below the light-line, where $\gamma_c \sim 0$.

There has been extensive work in SC with J-aggregates due to their high oscillator strength and photoluminescence [21, 68, 88]. However, 2D atomic crystals naturally stack forming slabs and given their high refractive index they can sustain FP modes with low radiative losses, meaning that $\gamma_c \to \gamma_0$ for both guided and FP modes. This makes them interesting for self-hybridizing to form polaritons. In fact, polaritons with FP modes in TMDs have been optically measured above the light-line [17, 89].

Polaritons below the light-line in MoS_2

The optical modes below the light-line have been overlooked by the strong coupling community until very recently [90–92]. In the usual FP cavities used in experiments that have measured polaritonic induced changes in materials properties, only one FP resonance is considered, that resonance is tuned to the material resonance. The changes are measured when $\delta \sim 0$ to the specific FP mode and compared to the detuned case [8].

Nevertheless, below the light-line, several modes can be in SC simultaneously (for various k_x), even when no FP mode matches the resonance, thus implying the importance of considering the modes coupled beyond the light-line. In a very recent work, where *cavity-free* organic molecules were measured beyond the light-line [93], it is pointed out that in previous works that used *traditional* polaritonic structures, there would exist polaritons beyond the light-line even if the external cavity would not be there.

Even though measurements below the light-line are more intricate, they have been recently measured via scattering-type scanning near-field optical microscope (s-SNOM) in WSe_2 [92] and hBN [91] slabs. Even more so, recent work has shown self-hybridized vibrational polaritons below the light-line in a $\alpha-$lactose photonic crystal [94].

Using a different approach, measurements of polaritons below the light-line in MoS_2 slabs are shown here. For this, flakes of MoS_2 with different thicknesses in various regions were exfoliated and transferred onto a glass substrate (see Methods section 5.2.2). The measured regions are labeled in the bright field image of the flake shown in transmission in figure 4.3(a). The colors in the bright field are given by the FP modes formed by the flake. When imaging the Fourier plane of those flakes in reflection beautiful colors are seen. The colors depend on the FP resonance wavelength (figure 4.3(i)). The Fourier plane expands the angular information of the reflected light. Light reflected at normal incidence is focused in the center of the circles and the higher the angle (or $k_x = n \sin\theta$) the further away from the center. For details on the Fourier imaging technique for angular resolution see Methods section 5.3.1.

The limit of the light-line in air is where the bright inner circle can be seen. The purple area in figure 4.3(b,i), between the center of the circle and the bright circle, is given by the FP resonances. After the bright circle and before the edge of the circle, there are several colors changing rapidly from blue to yellow. That part is given by modes below the light-line leaking.

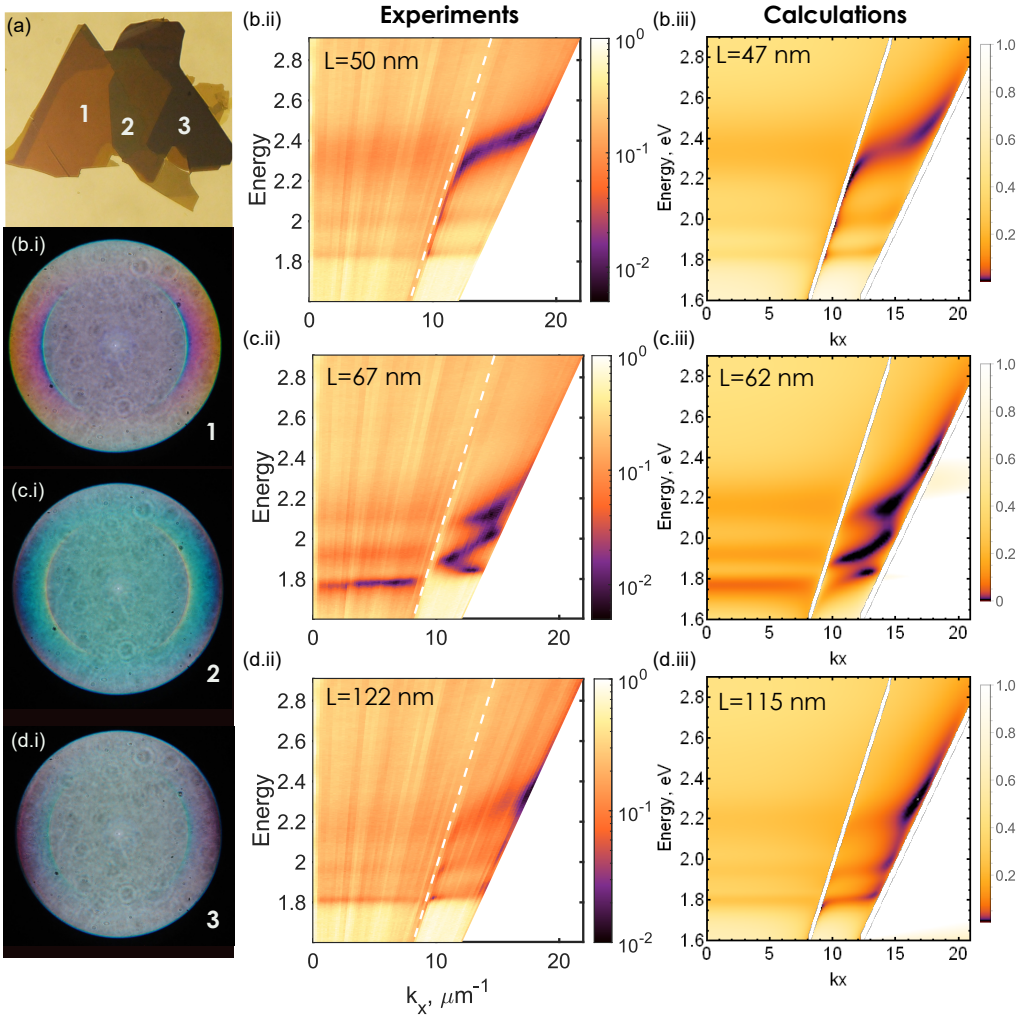

FIGURE 4.3: (a) Bright field image of the measured MoS_2 flake with different thicknesses. (i) Fourier plane images. (ii) Dispersion in reflection measurements and (iii) calculations for different thicknesses (b) $L = 50 \pm 5$ nm experimental, calculation for $L = 47$ nm, (c) $L = 67 \pm 5$ nm, calculation for $L = 62$ nm and (d) $L = 122 \pm 5$ nm and calculation for $L = 115$ nm. The differences in thickness are due to inaccuracies in the measurement.

The second column (ii) of figure 4.3 shows the spectral resolution of the images shown in (i) for TM polarization. These are dispersion plots above and below the light-line (dotted white line in (ii)).

Above the light-line in figure 4.3(b,ii) there is a broad area almost horizontal around 2.37 eV given by the FP resonance. This resonance is blue-detuned from both A and B excitons. Nonetheless, in 4.3(c,ii) the FP is tuned to the excitons, giving rise to polaritons above the light line. Moreover, while the guided mode in (b,ii) is blue-detuned from the excitons, the mode below the light-line in (c,ii) is strongly coupled to both A and B excitons, generating a splitting with each of them.

The thicknesses of the flakes were measured by AFM and calculations (see Methods 5.1) were made using them as an input to match the measured spectra. The regions with perfect absorption depend strongly on the thickness, so they can be used to approximate L better in the calculations.

The calculations allow to obtain the *bare* optical resonances to determine ω_c and γ_c accurately. More importantly, they open up the possibility for future studies of the

modes as in our previous work [85].

The characterization of the poles will be done in the future, but considering the bulk Rabi splitting of both A and B excitons (see Table 4.1) and the reflectivity experiments and calculations, the slabs are in SC both below and above the light-line.

4.2.2 1D polaritons in infinite cylinders

Next, the system is confined in one more dimension, giving rise to an infinite cylinder. Polaritons have been previously demonstrated in several perovskite nanowires [95, 96]. In [85] the case of an infinite cylinder was considered, it was shown that the optical resonances described in section 2.2.2 hybridize with the electronic transition in the perovskite $CsPbCl_3$.

This material is described by a Lorentz permittivity with $\varepsilon_\infty = 3.7$, $\omega_0 = 3$ eV, $\gamma_0 = 87$ meV, and $f\omega_P^2 = 0.54$ eV^2 [50]. Giving a bulk Rabi splitting of 0.382 eV $> \gamma_0/2$. The cylinders are strongly coupled both above and below the light-line , as showed by the trajectories.

An exciting recent study measured self-hybridized nanowires of organic semiconductors (J-aggregates and H-aggregates) [97]. Moreover, they showed that the polaritons have 5 times higher energy transport velocity than the expected for a non-polaritonic exciton [97]. Interestingly, they only resolved Rabi splitting (above the light-line) in about $\sim 30\%$ of the regions they measured[3], but always measured the transport effect. This may be related to the fact that the nanowires are strongly coupled also with guided modes below the light-line.

These observations highlight the importance of self-hybridized polaritons and of considering also the interaction with guided modes.

4.2.3 Polaritons in water spheres

Let us finally consider a sphere. In this case, the resonances are given by the Mie resonances described in Section 2.2.3. A theoretical study by Platts et al. [16] showed that GaAs spheres sustained polaritons. Here, being such a common material, the interest is to show self-hybridized water.

Recently, the polaritonic chemistry community has had a growing interest in water *traditional* polaritons for catalytic applications [98–101]. From the theoretical studies trying to understand such experiments, one found differences in rotational dynamics in water when in USC and uncoupled case [102].

In the appended paper, the coupling of the O-H stretch (figure 2.2) was studied. The study of scattering of water droplets has been extensive and is even used as example for text books [38]. Thus, it is a problem with well known solutions. Nevertheless, it gets interesting when paying additional attention to the spectral range covering O-H stretch in water molecules (wavelength $\sim 3\mu m$).

In the appended paper it was shown that water droplets self-hybridize and can reach USC. The *anticrossing* was plotted for different Mie modes. Here, the case of $TM_{1,2}$ is reproduced in figure 4.4(a). The trajectories show the splitting too, even with a more complex trajectory of the uncoupled mode.

[3] The authors attribute this to potential variations in the oscillator strengths.

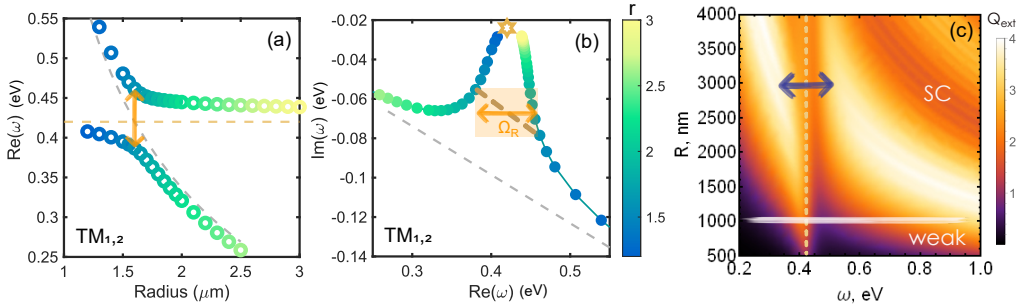

FIGURE 4.4: (a) Anticrossing of water O-H stretch resonance and $TM_{1,2}$ (electric dipole: $a_{l=1,N=2}$) Mie resonance by varying the sphere radius, R. Uncoupled values are shown in dashed curves. (b) Trajectories of water polaritonic QNMs with $TM_{1,2}$. The uncoupled Mie resonance is shown in a dashed line and the phonon in a star. (c) Extinction efficiency, Q_{eff}, of the droplets variation with radius. The white line shows the critical radius for having polaritons. The purple arrow shows the visible splitting. Figure modified from [85]

These first modes have large γ_c (see figure 2.8), for $TE_{1,1}$ it is so large that the coupling is weak. This means that modes with higher orbital, l, and radial numbers, N, couple even more strongly because $\gamma_c \to \gamma_0$. The challenge is that $\omega_c \propto l/R$ [16], thus the higher the orbital number the larger the sphere has to be to sustain a resonance in ω_0. Thus, there is a minimal droplet radius that sustains resonances than can achieve SC. In the case of water that radius is $R \sim 1.1\ \mu m$.

In general, it is hard to excite a single mode in spheres [103], meaning that an incoherent superposition of all the modes will be measured. As is the case in extinction measurements (figure 2.8(b)), where there is a maximum of extinction around $\omega_0 = 0.42$ eV for $R \sim 3\ \mu m$. Figure 4.4(c) shows the extinction efficiency for the interaction. Around $R \sim 3\ \mu m$ there is a visible splitting of ~ 0.22 eV marked with an arrow. This splitting can be misleading, as this is not exactly a *Rabi* splitting, but the result of the incoherent sum of the extinction of all modes of the droplet.

Figure 4.4(c) shows that below the white line $\sim 1\ \mu m$, the extinction has a maximum on the ω_0, so those droplets are only weakly coupled as mentioned above. Then an interesting point is that, such sizes of water droplets exist in nature in fogs and clouds [104]. The size distribution depends on the type of the fog or cloud [105]. This could mean that some of them are polaritonic and some are not.

4.3 The limits of the coupling

4.3.1 Critical Size

The previous section pointed out that not all sizes in droplets sustain Mie resonances can hybridize with the O-H stretch in water. This gives a clear critical size for polaritons to exist in water spheres, such that larger radii sustain polaritons but smaller don't. In the appended study, polaritons with a critical size were shown in all the studied geometries and materials. The critical radii depends on ω_0 and the material's background permittivity [16]. The higher ε_∞, the smaller the spheres can be to sustain polaritons.

This limiting factor for sustaining modes to self-hybridize is general for all the studied structures. In planar and cylindrical structures, the limit is given by the

TABLE 4.1: Calculated values of the bulk Rabi splitting, $2g_0$, η and the minimal slab thickness needed to sustain polaritons, L_{min}.

Material	$2g_0$ **(eV)**	η	L_{min} **(nm)**
Water	0.1	0.12	1373
hBN	0.12	0.35	2.56
Perovskite ($CsPbCl_3$)	0.382	0.06	4.35
J-aggregates low f	0.455	0.11	9.75
J-aggregates high f	1.204	0.29	3.68
MoS_2 A-exciton	0.328	0.09	2.38
MoS_2 B-exciton	0.524	0.13	2.14

first guided modes. Even for cylinders, where the HE_{11} mode has no cut-off, the mode becomes too lossy to sustain polaritons for very small radii. Thus, there is a minimal size for structures to sustain polaritons.

In the appended there is a rough approximation of the minimal thickness that could sustain polaritons below the light-line for the 1st TE mode in slabs.

$$L_{min}^2 > \frac{\gamma^2}{2k_0^2(f\omega_P^2)\sqrt{\varepsilon_\infty - 1}} \,. \tag{4.4}$$

In this case, k_0 is the wave vector in vacuum at which $\delta = 0$. This results in different thicknesses for different materials (see table 4.1), this is a rough guideline to look for polaritonic vs non-polaritonic slabs. Here the structures are considered in vacuum, the critical sizes will vary in a different medium (e.g., placing it on a substrate). Of course, by matching the surrounding media refractive index with the structure the optical resonances disappear (and so do polaritons).

4.3.2 Maximum Rabi splitting

For all the materials and optical resonances analyzed, the Rabi splitting, Ω_R was always below the Bulk Rabi splitting, $2g_0$. Table 4.1 shows a summary of Bulk Rabi splittings for all the studied materials. The table also shows that some of these materials can even reach the USC regime, $\eta > 0.1$.

This gives an easy guideline when looking for materials that can be strongly coupled. For such an estimation it would suffice to know the permittivity (or refractive index) and to fit a Lorentzian (equation 2.5) to the resonance of interest. Then, it is easy to check for the existence of polaritons with $f\omega_P^2 > \varepsilon_\infty\gamma^2/4$.

Summarizing, Lorentz materials do not need an external cavity to form polaritons. It is possible to reshape the material itself to sustain optical modes with the desired characteristics. The capability of the material to form polaritons only depends on its own optical properties. Even more so, since the bulk polaritons seems to be the maximum attainable Rabi splitting, it is only necessary to fit a Lorentzian to the resonance of interest and calculate $2g_0 = \omega_P\sqrt{f/\varepsilon_\infty}$ to know if it will be possible to achieve SC or even USC.

As described in this chapter, the community is starting to pay attention to cavity-free self-hybridized polaritons and their potential to change materials properties [93, 94, 97]. Moreover, self-hybridized polaritons are a unique platform

for understanding such changes (particularly for polaritonic chemistry) because they provide polaritons without extra interactions given by the material of the external cavity. This helps to isolate the impact of the polaritons when measuring the materials properties.

Chapter 5

Research methods

The previous chapters have described the theory, previous works and my contributions to the field without going deeply into the methods. Thus, this chapter focuses on the details used for the calculations, the fabrication and optical measurements techniques used in this thesis.

5.1 Analytical Calculations

Hopfield Hamiltonian solutions

The Hopfield Hamiltonian was discussed in Section 3.2.1, here it is only discuss how the eigenfrequencies were obtained for figure 3.5. The eigenvalue problem is given by

$$[\hat{\alpha}, \hat{H}] = \hbar\omega_{\pm}\hat{\alpha} \ , \tag{5.1}$$

where the eigenfunctions are the polariton operator $\hat{\alpha} = w\hat{a} + x\hat{b} + y\hat{a}^{\dagger} + z\hat{b}^{\dagger}$. Then, eq. 3.2 can be rewritten in matrix form as [12]:

$$\hbar \begin{bmatrix} \omega_c(\theta) + 2\frac{g^2}{\omega_0} & -\mathrm{i}g & -2\frac{g^2}{\omega_0} & -\mathrm{i}g \\ \mathrm{i}g & \omega_0 & -\mathrm{i}g & 0 \\ 2\frac{g^2}{\omega_0} & -\mathrm{i}g & -\omega_c(\theta) - 2\frac{g^2}{\omega_0} & -\mathrm{i}g \\ -\mathrm{i}g & 0 & \mathrm{i}g & -\omega_0 \end{bmatrix} \begin{bmatrix} w \\ x \\ y \\ z \end{bmatrix} = \hbar\omega_{\pm} \begin{bmatrix} w \\ x \\ y \\ z \end{bmatrix} \tag{5.2}$$

This is the matrix problem solved for various angles of incidence, θ, to obtain $\omega_{\pm}$ in figure 3.5. The coupling strength, g, for TE was considered fixed for all angles and was obtained experimentally from the minimal distance between the two polaritonic resonances dips $g = \Omega_R/2$. The theoretical value of the coupling strength for this system can be found in equation 3.6.

Cavity-free polaritons calculations

Quasinormal modes in open systems

Chapter 2.2 described resonances in dielectric systems with different geometrical shapes. There the concept of a *quasinormal mode* (QNM) was introduced. As mentioned there, all the calculations considered open systems, with radiative losses to the environment. Both, the modes in closed systems and QNMs in open systems, are solutions to the the source-less Maxwell's equations. The main

difference is given by the boundary conditions. In the case of open systems the system should obey the Silver-Müller (SM) radiation conditions, which state that there should be no sources of radiation in the far-field, such that the energy flow is only outgoing [49].

Let us consider the source-less Maxwell's equations with no free charges in a matrix form that obey the Silver-Müller conditions, such that they look like an eigenvalue problem (equation 5.3) [48]:

$$\begin{bmatrix} 0 & \mathrm{i}\varepsilon^{-1}(\mathbf{r},\tilde{\omega})\nabla\times \\ -\mathrm{i}\mu^{-1}(\mathbf{r},\tilde{\omega})\nabla\times & 0 \end{bmatrix} \begin{bmatrix} \tilde{\mathbf{E}}(\mathbf{r}) \\ \tilde{\mathbf{H}}(\mathbf{r}) \end{bmatrix} = \tilde{\omega} \begin{bmatrix} \tilde{\mathbf{E}}(\mathbf{r}) \\ \tilde{\mathbf{H}}(\mathbf{r}) \end{bmatrix}. \tag{5.3}$$

The Silver-Müller radiation conditions for scattering calculations, where an incoming field interacts with a structure, are such that only the scattered field needs to obey the SM radiation conditions. After some simplifications it means that $\hat{\mathbf{r}} \cdot \mathbf{E}(\mathbf{r},\omega)$ vanishes at large distances.

The solutions of the open system are the so-called *quasinormal modes* (QNMs). The eigenvectors are the QNMs' spatial field distributions $[\tilde{\mathbf{E}}(\mathbf{r}), \tilde{\mathbf{H}}(\mathbf{r})]$ and the eigenvalues are its complex frequencies, $\tilde{\omega}_n = \omega_n - \mathrm{i}\gamma_n/2$ [48, 49]. As explained before, the real part is the measurable resonant frequency, ω_n, and the imaginary part is the decay rate, associated to its lifetime, $\tau_n = 1/\gamma_n$. This means that the field decays exponentially with time, $\mathbf{E}(\mathbf{r},t) = \tilde{\mathbf{E}}(\mathbf{r})e^{\mathrm{i}\omega_n t}e^{-\gamma_n t}$, and similarly for $\mathbf{H}$.

Among the various methods to find QNMs [48, 49], it is possible to compute them by searching poles in the complex ω plane of the system's electromagnetic response [106]. For the 3 simple geometries studied here, it is possible to analytically calculate the reflectivity or extinction cross-sections and look for divergences in the complex plane. The following sections describe the details for the calculations in each geometry.

For this reason, the QNMs throughout the text are shown as poles $\mathrm{Re}(\tilde{\omega})$ vs $\mathrm{Im}(\tilde{\omega})$ plots. The cavity QNMs, were obtained with $\varepsilon = \varepsilon_\infty$, whereas the QNMs for polaritons where obtained considering a Lorentzian permittivity (equation 2.5). The values for the various materials are found in table 5.1. Next, the specific characteristic equations used for each geometry to find the QNMs are described.

Dielectric slabs

To obtain the eigenvalues the poles of the reflection coefficient are found for either TE or TM polarization. For that, the Fresnel reflection and transmission coefficients are used [15].

Considering the incoming light, $\mathbf{E}_{in}$, with an angle, $k_x = k_0 \sin\theta$. With k_0 the wave vector in vacuum. Then the incoming and scattered light can be described as,

$$\mathbf{E}_{in}(\mathbf{r}) = a_1\mathbf{E}e^{\mathrm{i}k_z z + \mathrm{i}k_x x} + a_2\mathbf{E}e^{-\mathrm{i}k_z z + \mathrm{i}k_x x} \tag{5.4}$$

$$\mathbf{E}_{scat}(\mathbf{r}) = b_1\mathbf{E}e^{-\mathrm{i}k_z z + \mathrm{i}k_x x} + b_2\mathbf{E}e^{\mathrm{i}k_z z + \mathrm{i}k_x x} \tag{5.5}$$

The reflection coefficient can be obtained from 5.4 using the TMM method [35]:

TABLE 5.1: Values for the permittivities with Lorentz model used for the various materials used for cavity-free polaritons calculations

Material	ε_∞	f_0	ω_0 (eV)	γ (eV)
Perovskite	3.7	0.06	3	0.087
hBN	4.45	2.24	0.169	0.001
water	1.75	0.1	0.42	0.048
J-aggregates low f	2.15	0.1	2.11	0.1
J-aggregates high f	2.15	0.7	2.11	0.1

$$R_{\mathrm{TE,TM}} = \frac{r_{\mathrm{TE,TM}}(1 - e^{2\mathrm{i}k_{z,2}L})}{1 - r^2_{\mathrm{TE,TM}} e^{2\mathrm{i}k_{z,2}L}}, \tag{5.6}$$

where,

$$r_{\mathrm{TE}} = \frac{k_{z,1} - k_{z,2}}{k_{z,1} + k_{z,2}}, \quad r_{\mathrm{TM}} = \frac{k_{z,1} - k_{z,2}/\varepsilon(\omega)}{k_{z,1} + k_{z,2}/\varepsilon(\omega)}, \tag{5.7}$$

with $k_{z,1} = \sqrt{k_0^2 - k_x^2}$, $k_{z,2} = \sqrt{\varepsilon(\omega)k_0^2 - k_x^2}$ being the z-components of the wave vector in vacuum and dielectric, respectively.

The poles of the system are the roots of the characteristic equation:

$$1 - r^2_{\mathrm{TE,TM}} e^{2\mathrm{i}k_{z,2}L} = 0\,. \tag{5.8}$$

The analytical calculations of MoS_2 slabs shown in figure 4.3 were done with the same procedure as slabs in vacuum, but the medium on the light incidence side had refractive index of $n = 1.51$.

For the calculations a Lorentz material was considered with 3 resonances given by the A, B and C excitons to fit the experimental permittivity showed in fig 2.3(b) for bulk MoS_2 [29]:

$$\varepsilon(\omega) = \varepsilon_\infty + \sum_{i=1}^{3} f_i \frac{\omega_{P,i}^2}{\omega_{0,i}^2 - \omega^2 - i\gamma_i\omega} \tag{5.9}$$

Where, $\varepsilon_\infty = 12$, $\omega_{0,1} = 1.845$ eV, $\gamma_{0,1} = 0.07$ eV, $f_1\omega_{P,1}^2 = 1.29$ eV^2, $\omega_{0,2} = 2.03$ eV, $\gamma_{0,2} = 0.17$ eV, $f_2\omega_{P,2}^2 = 3.30$ eV^2, $\omega_{0,2} = 2.75$ eV, $\gamma_{0,2} = 0.63$ eV, $f_2\omega_{P,2}^2 = 52.94$ eV^2.

Infinite cylinders

Now let us consider a wave propagating through an infinite dielectric cylinder with radius a, propagating in $\hat{z}$ direction. In this geometry it is convenient to use cylindrical coordinates (ρ, ϕ, z). For TE (TM) polarization, all the **E** (**H**) fields are transverse to z. However, the analysis of TE and TM in this case is tricky, because it is only possible to separate TE and TM when there is no azimuthal variation, i.e., when $m = 0$.

The exact solutions of the fields inside and outside of the cylinder are beyond the scope of this text, but the reader can find an explicit description in [51]. Here there is just an intuitive description the final results. Inside the cylinder, $\rho < a$, the field behaves as Bessel functions: $E_z \propto J_m(k_{\rho,2}\rho)e^{\mathrm{i}m\phi}e^{\mathrm{i}\beta z}$. Outside of the cylinder, $\rho > a$,

$E_z \propto H_m^{(1)}(k_{\rho,1}\rho)e^{\mathrm{i}m\phi}e^{\mathrm{i}\beta z}$. The radial component of the wave vectors outside and inside the cylinder are $k_{\rho,1} = \sqrt{k_0^2 - k_z^2}$ and $k_{\rho,2} = \sqrt{\varepsilon(\omega)k_0^2 - k_z^2}$, respectively.

Then, the characteristic equation is obtained by considering the continuity of the field at $\rho = a$ [51, 107]:

$$\left[\frac{1}{k_{\rho,2}}\frac{J_m'\left[k_{\rho,2}a\right]}{J_m\left(k_{\rho,2}a\right)} - \frac{1}{k_{\rho,1}}\frac{H_m^{(1)'}\left(k_{\rho,1}a\right)}{H_m^{(1)}\left(k_{\rho,1}a\right)}\right]\left[\frac{\varepsilon}{k_{\rho,2}}\frac{J_m'\left(k_{\rho,2}a\right)}{J_m\left(k_{\rho,2}a\right)} - \frac{1}{k_{\rho,1}}\frac{H^{(1)'}m\left(k_{\rho,1}a\right)}{H_m^{(1)}\left(k_{\rho,1}a\right)}\right] = \left[\frac{mk_zk_0(\varepsilon-1)}{a^2k_{\rho,1}k_{\rho,2}}\right]^2. \quad (5.10)$$

From this equation is visible that TE and TM are usually mixed. The QNMs are considered hybrid and are named EH_{ml} and HE_{ml}. Nevertheless, for $m = 0$ there are separate characteristic equations for TE and TM:

$$\frac{\varepsilon}{k_{\rho,2}}\frac{J_1'(k_{\rho,2}a)}{J_1(k_{\rho,2}a)} - \frac{1}{k_{\rho,1}}\frac{H_1'(k_{\rho,1}a)}{H_1(k_{\rho,1}a)} = 0, \quad \text{(TM)} \quad (5.11)$$

$$\frac{1}{k_{\rho,2}}\frac{J_1'(k_{\rho,2}a)}{J_1(k_{\rho,2}a)} - \frac{1}{k_{\rho,1}}\frac{H_1'(k_{\rho,1}a)}{H_1(k_{\rho,1}a)} = 0. \quad \text{(TE)} \quad (5.12)$$

Spheres

Now let us consider spherical coordinates (r, θ, ϕ) and sphere of radius R in vacuum. Here the Mie theory solutions derived in [38] are used.

The field scattered by a sphere of radius R and permittivity $\varepsilon = n^2$ can be written as an infinite series of spherical vector harmonics with scattering coefficients a_l and b_l [38].

$$a_l = \frac{n\psi_l(nx)\psi_l'(x) - \psi_l(x)\psi_l'(nx)}{n\psi_l(nx)\xi_l'(x) - \xi_l(x)\psi_l'(nx)}, \quad (5.13)$$

$$b_l = \frac{\psi_l(nx)\psi_l'(x) - n\psi_l(x)\psi_l'(nx)}{\psi_l(nx)\xi_l'(x) - n\xi_l(x)\psi_l'(nx)}, \quad (5.14)$$

where $x = k_0R$. The Ricatti-Bessel functions: $\psi_l(\rho) = \rho j_l(\rho)$ and $\xi_l(\rho) = \rho h_l^{(1)}(\rho)$ are used to simplify the expressions with spherical Bessel, $j_l(\rho)$, and first kind Hankel functions, $h_l^{(1)}(\rho)$.

The coefficient a_l (b_l) weighs the contribution of the l-th TM (TE) mode, for which there is no radial magnetic (electric) field. Thus, the eigenfrequencies for TE and TM polarized modes with orbital number l are found as roots of the following characteristic equations:

$$\psi_l(nx)\xi_l'(x) - n\xi_l(x)\psi_l'(nx) = 0, \quad \text{(TE)} \quad (5.15)$$

$$n\psi_l(nx)\xi_l'(x) - \xi_l(x)\psi_l'(nx) = 0. \quad \text{(TM)} \quad (5.16)$$

The hybrid modes between the optical modes and the vibrational or electronic transition were calculated by finding the poles of the same equations but using a

simple Lorentz model for the permittivity of each material with the values shown in table 5.1, where $f_0\omega_0^2 = f\omega_P^2$ in eq. 2.4.

5.2 Nanofabrication

This part describes the nanofabrication process for traditional polaritons of microcavities and plasmonic particles and self-hybridized MoS_2 slabs.

All the samples were prepared on glass coverlips (170 μm). Cleaned by 5 min ultrasonication in acetone and IPA, followed by oxygen plasma ashing.

5.2.1 Microcavities and plasmonic particles

The plasmon - microcavity polaritonic samples were fabricated by the following series of steps:

1. Bottom mirror evaporation: 2 nm Cr of adhesion layer were deposited with e-beam evaporator (Kurt J. Lesker PVD225), followed by evaporation of 30 nm Au.
2. Spacer: Half a cavity thickness: $L/2$ = 80, 85 and 90 nm of SiO_2 was deposited by STS plasma-enhanced chemical vapor deposition (PECVD) at 300 °C.
3. Nanodisk arrays: prepared by electron beam lithography (EBL). Therefore, spin coated PMMA (baked for 5 min at 180 °C) was used as positive resist to pattern 12 arrays of 50×50 μm with disks of diameters $d = 60, 80$ and 100 nm and different pitches $\Lambda = 100, 140, 180, 220, 300$ and 340 nm. After the development and oxygen plasma ashing of the exposed areas, 20 nm of Au are evaporated. Then lift-off in acetone finalizes the disks fabrication. To improve the crystallinity of the nanodisks, the samples were annealed for 10 min at 200 °C on a hotplate.
4. Spacer: the second part of the spacer thickness $L/2$ was PMMA spin coated on top of the Au nanoparticle array and baked at 180 °C for 5 min.
5. Top mirror evaporation: 30 nm Au layer deposited by e-beam evaporation.

Control samples (no cavity) of the nanodisk arrays were prepared as in step 3 on glass and imaged with SEM (Zeiss Supra 60 VP - EDX) by coating them with a thin layer of conductive polymer (E-spacer).

5.2.2 Transfer and characterization of 2D materials

MoS_2 flakes were mechanically exfoliated (popularly known as Schotch-tape method) from bulk crystals (HQ Graphene) with dicing tape and transferred to thin PDMS stamps. Finally, the flakes were transferred onto glass substrates following the procedure by Castellanos-Gomez et al. [108].

The monolayers were identified by their distinctive photoluminescence [32] in an upright Nikon microscope with a fiber-coupled spectrometer (Andor Shamrock SR-303i) equipped with a CCD (Andor iDus 420).

The optical pictures of the transferred flakes were taken with a Nikon D300S. Then the number of layers were deduced by optical contrast in the software ImageJ.

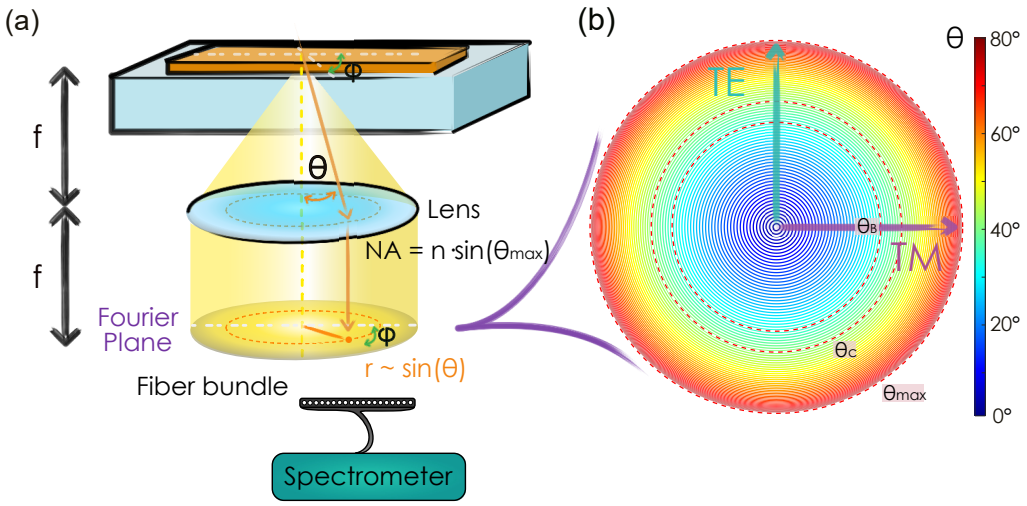

FIGURE 5.1: Fourier spectroscopy concept. (a) Schema of the experimental setup for angle resolution. Collimated light incident to the lens is focused in the sample, such that the incident light to the sample comes at all the angles up to $\theta_{max} = \arcsin NA/n$. The reflected signal is collected with the same lens. The Back Focal Plane (BFP) of the lens is then imaged and the spectra at different radii are collected simultaneously via a fiber bundle with a spectrometer. (b) Angular distribution of the BFP for an oil immersion objective with NA=1.49. Brewster, θ_B, and critical, θ_C, angles are marked in red dashed lines. The lines for TE and TM mark the locations to measure those polarizations.

Additionally, the thicknesses were also measured by AFM (NTEGRA Prima, NT-MDT) by Dr. Battulga Munhkbat in noncontact mode. The error bar of such measurements is high, thus the need of both characterization techniques for the thickness of the layers.

5.3 Optical characterization

The optical characterization of nano and microstructures throughout the text is heavily based on reflectivity measurements. In this part, normal incidence and dispersion (angular distribution) reflectivity are described.

Reflection spectra at normal incidence in figure 3.3 were collected using a 20× objective (Nikon, NA = 0.45) in an upright microscope with a fiber-coupled spectrometer (Andor Shamrock SR-303i) equipped with a CCD (Andor iDus 420). The reflection was normalized with a standard dielectric-coated silver mirror (Thorlabs).

5.3.1 Fourier spectroscopy

Fourier optics is a broad area of study [35], but here it is used only to measure the angular spectral information of the microcavity-plasmon coupled system (figs. 3.4 and 3.5) and of the MoS_2 slabs (figs. 2.5 and figure 4.3).

To obtain the angular information the Fourier plane (or Back Focal Plane, BFP) was imaged. The concept is sketched in figure 5.1(a), where the fact that any lens of focal length f generates the Fourier transform at a distance f is used [35]. An example is depicted in the schema, where incoming collimated light (only one k-vector) will

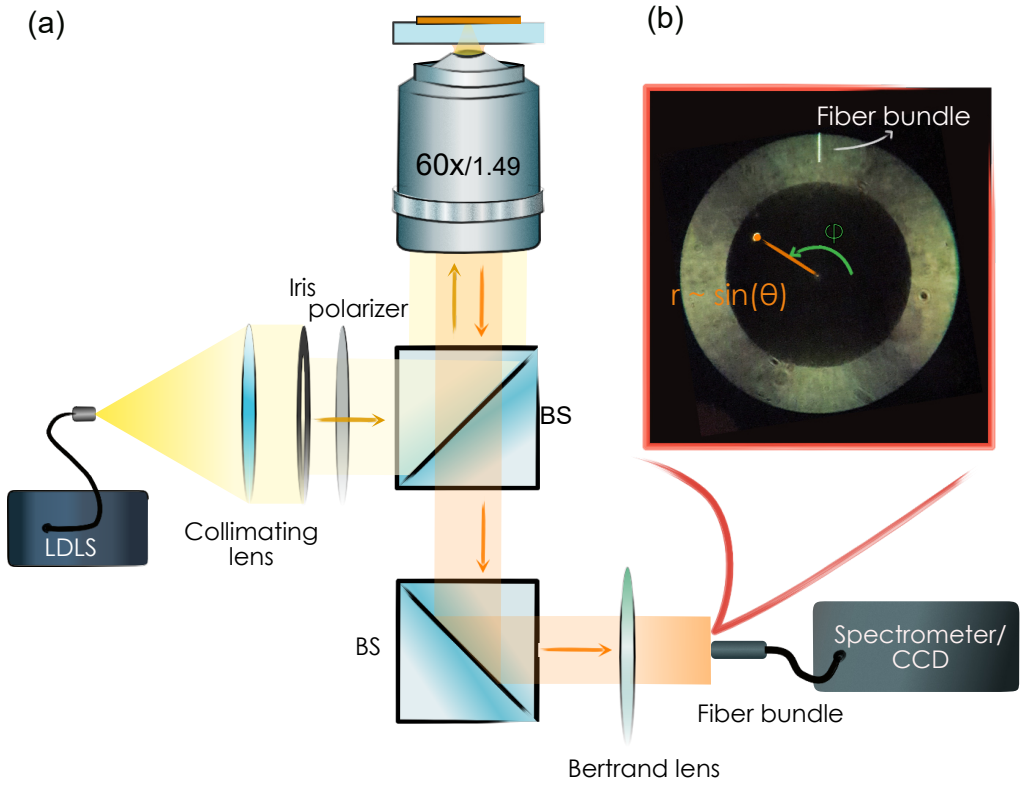

FIGURE 5.2: (a) Experimental setup for Fourier spectroscopy. Fiber coupled LDLS light is collimated and polarized before being redirected to the objective with a beam splitter (BS) in the inverted microscope. The reflected light from the sample (in orange) is redirected to a Bertrand lens to image the BFP in the spectrometer and a CCD simultaneously in different ports. of the microscope. (b) BFP image of glass showing the TIR area and the size of the fiber bundle in position to measure TE polarization.

be fully focused in a single point. Vice-versa, light reflected from the sample at different angles θ land in the BFP in different radii, $r \sim sin(\theta)$ [109].

The idea of Fourier spectroscopy for angular resolution is to image the BPF of the lens and to measure the spectra of the light at different radii. The information of the azimuthal angle, ϕ, is also available [110]. In this case, it is useful to characterize separately, the response of the sample to TE and TM polarized light, as shown in figure 5.1(b). It is also possible to measure any polarization mixture in between these two, where the weight of each polarization depends on the azimuthal angle as $E_{\text{TM}} \sim cos(\phi)$ and $E_{\text{TE}} \sim sin(\phi)$ [110].

The angles at which the lens collects light are limited by its numerical aperture, NA$= n \cdot \sin\theta_{max}$, where n is the refractive index of the medium[1] and θ_{max} is the maximum angle that the lens can collect light from. The sketch in figure 5.1(b) shows in different colors the radii corresponding to different angles for an oil immersion objective of NA=1.49. The outer most dashed circle corresponds to $\theta_{max} = 80.7°$. Two important angles are also in dashed lines, the Brewster angle, θ_B was used to characterize the minimal reflection measurable in our setup for to measure perfect absorption. The critical angle, θ_C, is the angle after which there is total internal reflection (TIR) in glass.

[1] Usually air, water or oil in commercial objectives.

A more accurate description of the optical setup for the MoS_2 measurements is shown in figure 5.2(a). An inverted microscope (Nikon Eclipse TE2000-E) was used to illuminate the sample with a collimated laser-driven white light source (LDLS, EQ-99FC, high-brightness, flat-broadband spectrum). The collimated and polarized light is focused in the sample with an oil (n=1.51) immersion 60× objective (Nikon, NA=1.49) to illuminate from the bottom.

The same objective collects the reflected light (depicted in orange) and redirects it with a beam splitter (BS) to the spectrometer or CCD camera. A Bertrand lens is used to image the Fourier plane of the objective[2]. Then the spectra for different radii is collected simultaneously with a fiber bundle consisting of 19 fibers with $100\ \mu m$ core (Andor SR-OPT-8002). The radii scale as $r \sim \sin\theta$ (figure 5.1(b)), thus if more angular resolution is needed at high angles, the BFP is expanded with a telescope as shown in figure 5.2(b).

Figure 5.2(b) shows the BFP image for a glass substrate, the bright area is given by the aforementioned TIR zone, $\theta \in [\theta_C, \theta_{max}]$. The lamp spectra in this area was used to normalize the measurements. This area is measurable only with an oil immersion objective that matches the refractive index of glass, thus allowing to measure leaky guided modes below the light-line (figure 4.3) and is also a Kretschmann configuration [36] to measure the SPP showed in figure 2.4.

The setup to measure above the light-line for the *traditional* polaritons dispersion in (figs. 3.4 and 3.5) is very similar to figure 5.2. But the objective and illumination source are different. In this case, an air 40× (NA=0.95) objective ($\theta_{max} = 71.8°$) was used and a fiber-coupled Halogen lamp (Thorlabs) to illuminate from the bottom.

[2]The BFP is usually inside the objective, so an external lens is required to image it.

Chapter 6

Concluding remarks

In this thesis, strong-light matter coupling was explored in two platforms. Firstly, in *traditional* polaritons, where a material transition resonance is coupled to an external cavity that sustains the optical modes. Secondly, in *cavity-free* polaritons, where both the material and the optical resonances are sustained by the same structure.

To obtain a full description, the beginning (Chapter 2) focused on the optical properties of materials. Describing mainly the permittivity of materials and their expression as a Lorentzian (section 2.1). As an example of the power of tailoring the optical response of structures, perfect absorption in just a few nm thick MoS_2 slabs was shown too. The second part of the chapter described optical resonators in dielectrics with different geometries: slabs, cylinders and spheres.

Chapter 3 gave a general description of light-matter interactions in different regimes: weak, strong and ultrastrong coupling. Then, an example of *traditional* polaritons was described in microcavity-plasmon coupling. This versatile platform allows to achieve strong and ultrastrong coupling in room temperature by tuning the nanodisk array parameters.

Chapter 4 started with a description of *bulk* polaritons, followed by a the concept of reshaping materials for them to sustain their own optical modes. This can generate *cavity-free* polaritons. The permittivity description discussed in section 2.1, was used to couple excitonic and phononic resonances to optical resonances described in section 2.2.

Finally, chapter 5 focused on the methods used through the thesis, including details on calculations, nanofabrication and optical characterization.

Outlook

As mentioned mainly in Chapter 4, the idea of cavity-free self-hybridized polaritons started slowly, with scattered works in slabs [17], perovskite cylinders [95], GaAs spheres [16] and TMDs Mie resonators [18]. Nevertheless, a renewed interest on cavity-free polaritons is growing fast, pushed largely by the interesting development of polaritonic chemistry. Now, recent works have measured Rabi splitting in slabs [93, 94]. Even more so, the typical energy transport in organic semiconductor cylinders has been attributed to polaritons[97].

Our appended work [85] has taken part on initiating this new wave of interest on the polaritonic properties without an external cavity. We showed that materials that sustain *bulk* polaritons can also self-hybridize with their own modes if the material is reshaped. We also showed that the *bulk Rabi splitting*, $2g_0$, is the

maximum Rabi splitting achievable for all the studied geometries. Moreover, it solely depends on the macroscopic optical properties of the bare material. This value can become a quick guideline for researchers to check if a certain material is suitable to sustain polaritons. Finally, we stressed the importance of modes below the light-line and the critical sizes to sustain polaritons. Additionally, we have experimentally measured polaritons in simple MoS_2 slabs, with a beautiful optical response in the Fourier plane.

My future work will focus on cavity-free structures and their properties, and probably many others will join. My interest resides on the role of the external cavities in the changes observed experimentally before [8]. Intriguing questions are now on the table. As recently put by Thomas et. al. [93], it is interesting to note that for some of the previous *traditional* experimental results, the polaritons beyond the light-line never disappear when removing the external cavity. Thus, the changes in material properties measured in *traditional* polaritonic platforms [8] should be expected also in *cavity-free* platforms. Moreover, *cavity-free* platforms allow to study polaritons without the external cavity restricting access to the material. They have potential to show the impact of polaritons in simpler experiments.

Bibliography

1. Peters, V. N., Prayakarao, S., Koutsares, S. R., Bonner, C. E. & Noginov, M. A. Control of Physical and Chemical Processes with Nonlocal Metal–Dielectric Environments. *ACS Photonics* **6,** 3039–3056 (2019).
2. Hutchison, J. A., Schwartz, T., Genet, C., Devaux, E. & Ebbesen, T. W. Modifying chemical landscapes by coupling to vacuum fields. *Angewandte Chemie International Edition* **51,** 1592–1596 (2012).
3. Munkhbat, B., Wersäll, M., Baranov, D. G., Antosiewicz, T. J. & Shegai, T. Suppression of photo-oxidation of organic chromophores by strong coupling to plasmonic nanoantennas. *Science Advances* **4,** eaas9552. ISSN: 2375-2548 (2018).
4. Ebbesen, T. W. Hybrid light–matter states in a molecular and material science perspective. *Accounts of Chemical Research* **49,** 2403–2412 (2016).
5. Feist, J., Galego, J. & Garcia-Vidal, F. J. Polaritonic chemistry with organic molecules. *ACS Photonics* **5,** 205–216 (2018).
6. Bhatt, P., Kaur, K. & George, J. Enhanced Charge Transport in Two-Dimensional Materials through Light–Matter Strong Coupling. *ACS nano* (2021).
7. Coles, D. M. *et al.* Polariton-mediated energy transfer between organic dyes in a strongly coupled optical microcavity. *Nature materials* **13,** 712–719 (2014).
8. Garcia-Vidal, F. J., Ciuti, C. & Ebbesen, T. W. Manipulating matter by strong coupling to vacuum fields. *Science* **373** (2021).
9. Törmä, P. & Barnes, W. L. Strong coupling between surface plasmon polaritons and emitters: a review. *Reports on Progress in Physics* **78,** 013901 (2014).
10. Hakala, T. K. *et al.* Bose–Einstein condensation in a plasmonic lattice. *Nature Physics* **14,** 739–744 (2018).
11. Anton-Solanas, C. *et al.* Bosonic condensation of exciton–polaritons in an atomically thin crystal. *Nature materials,* 1–7 (2021).
12. Hopfield, J. Theory of the contribution of excitons to the complex dielectric constant of crystals. *Physical Review* **112,** 1555 (1958).
13. Hopfield, J. Resonant scattering of polaritons as composite particles. *Physical Review* **182,** 945 (1969).
14. Henry, C. & Hopfield, J. Raman scattering by polaritons. *Physical Review Letters* **15,** 964 (1965).
15. Jackson, J. D. *Classical Electrodynamics* 3rd (John Wiley and Sons, Inc., New York, 1999).
16. Platts, C. E. *et al.* Whispering-gallery exciton polaritons in submicron spheres. *Physical Review B* **79,** 245322. ISSN: 10980121 (2009).
17. Munkhbat, B. *et al.* Self-Hybridized Exciton-Polaritons in Multilayers of Transition Metal Dichalcogenides for Efficient Light Absorption. *ACS Photonics* **6,** 139–147. ISSN: 23304022 (2019).

18. Verre, R. *et al.* Transition metal dichalcogenide nanodisks as high-index dielectric Mie nanoresonators. *Nature Nanotechnology* **14,** 679–684. ISSN: 17483395 (2019).
19. Fox, M. *Optical properties of solids* (American Association of Physics Teachers, 2002).
20. Collins, R. W. & Ferlauto, A. S. Optical physics of materials. *ChemInform* **37** (2006).
21. Balasubrahmaniyam, M, Genet, C. & Schwartz, T. Coupling and Decoupling of Polaritonic States in Multimode Cavities. *arXiv preprint arXiv:2005.03527* (2020).
22. Hale, G. M. & Querry, M. R. Optical Constants of Water in the 200-nm to 200-μm Wavelength Region. *Appl. Opt.* **12,** 555–563 (1973).
23. Segelstein, D. J. *The complex refractive index of water* PhD thesis (University of Missouri–Kansas City, 1981).
24. Novoselov, K. S. *et al.* Two-dimensional atomic crystals. *Proceedings of the National Academy of Sciences* **102,** 10451–10453. ISSN: 0027-8424 (2005).
25. Manzeli, S., Ovchinnikov, D., Pasquier, D., Yazyev, O. V. & Kis, A. 2D transition metal dichalcogenides. *Nature Reviews Materials* **2,** 1–15 (2017).
26. Geim, A. K. & Grigorieva, I. V. Van der Waals heterostructures. *Nature* **499,** 419–425 (2013).
27. Caldwell, J. D. *et al.* Photonics with hexagonal boron nitride. *Nature Reviews Materials* **4,** 552–567 (2019).
28. Caldwell, J. D. *et al.* Low-loss, infrared and terahertz nanophotonics using surface phonon polaritons. *Nanophotonics* **4,** 44–68. ISSN: 21928606 (2015).
29. Li, Y. *et al.* Measurement of the optical dielectric function of monolayer transition-metal dichalcogenides: MoS 2, Mo S e 2, WS 2, and WS e 2. *Physical Review B* **90,** 205422 (2014).
30. Van Baren, J. *et al.* Stacking-dependent interlayer phonons in 3R and 2H MoS2. *2D Materials* **6,** 025022 (2019).
31. Ermolaev, G. A. *et al.* Giant optical anisotropy in transition metal dichalcogenides for next-generation photonics.
32. Splendiani, A. *et al.* Emerging photoluminescence in monolayer MoS2. *Nano letters* **10,** 1271–1275 (2010).
33. Li, X.-L. *et al.* Layer-number dependent optical properties of 2D materials and their application for thickness determination. *Advanced Functional Materials* **27,** 1604468 (2017).
34. Johnson, P. B. & Christy, R.-W. Optical constants of the noble metals. *Physical review B* **6,** 4370 (1972).
35. Hecht, E. & Zajac, A. *Optics* (Addison Wesley San Francisco, 2002).
36. Maier, S. A. *Plasmonics: fundamentals and applications* (Springer Science & Business Media, 2007).
37. Yu, R., Liz-Marzán, L. M. & de Abajo, F. J. G. Universal analytical modeling of plasmonic nanoparticles. *Chemical Society Reviews* **46,** 6710–6724 (2017).
38. *Absorption and scattering of light by small particles* 530. ISBN: 3527618163 (Wiley, 2004).
39. Baranov, D. G., Krasnok, A., Shegai, T., Alù, A. & Chong, Y. Coherent perfect absorbers: linear control of light with light. *Nature Reviews Materials* **2,** 1–14 (2017).
40. Song, H. *et al.* Nanocavity absorption enhancement for two-dimensional material monolayer systems. *Optics express* **23,** 7120–7130 (2015).

41. Baranov, D., Edgar, J. H., Hoffman, T., Bassim, N. & Caldwell, J. D. Perfect interferenceless absorption at infrared frequencies by a van der Waals crystal. *Physical Review B* **92,** 201405 (2015).
42. Luo, J., Li, S., Hou, B. & Lai, Y. Unified theory for perfect absorption in ultrathin absorptive films with constant tangential electric or magnetic fields. *Physical Review B* **90,** 165128 (2014).
43. Bahauddin, S. M., Robatjazi, H. & Thomann, I. Broadband absorption engineering to enhance light absorption in monolayer MoS2. *Acs Photonics* **3,** 853–862 (2016).
44. Liu, J.-T., Wang, T.-B., Li, X.-J. & Liu, N.-H. Enhanced absorption of monolayer MoS2 with resonant back reflector. *Journal of Applied Physics* **115,** 193511 (2014).
45. Vahala, K. J. Optical microcavities. *nature* **424,** 839–846 (2003).
46. Baranov, D. G., Wersäll, M., Cuadra, J., Antosiewicz, T. J. & Shegai, T. Novel Nanostructures and Materials for Strong Light–Matter Interactions. *ACS Photonics* **5,** 24–42 (2018).
47. Heylman, K. D. *et al.* Optical microresonators for sensing and transduction: a materials perspective. *Advanced Materials* **29,** 1700037 (2017).
48. Lalanne, P., Yan, W., Vynck, K., Sauvan, C. & Hugonin, J.-P. Light interaction with photonic and plasmonic resonances. *Laser & Photonics Reviews* **12,** 1700113 (2018).
49. Kristensen, P. T., Herrmann, K., Intravaia, F. & Busch, K. Modeling electromagnetic resonators using quasinormal modes. *Advances in Optics and Photonics* **12,** 612–708 (2020).
50. Tiguntseva, E. Y. *et al.* Tunable hybrid Fano resonances in halide perovskite nanoparticles. *Nano Letters* **18,** 5522–5529 (2018).
51. Ishimaru, A. *Electromagnetic wave propagation, radiation, and scattering: from fundamentals to applications* (John Wiley & Sons, 2017).
52. Purcell, E. M., Torrey, H. C. & Pound, R. V. Resonance absorption by nuclear magnetic moments in a solid. *Physical review* **69,** 37 (1946).
53. Wallraff, A. *et al.* Strong coupling of a single photon to a superconducting qubit using circuit quantum electrodynamics. *Nature* **431,** 162–167 (2004).
54. Guebrou, S. A. *et al.* Coherent emission from a disordered organic semiconductor induced by strong coupling with surface plasmons. *Physical review letters* **108,** 066401 (2012).
55. Toepfer, J. D. *et al.* Engineering spatial coherence in lattices of polariton condensates. *Optica* **8,** 106–113 (2021).
56. Thomas, A. *et al.* Ground-State Chemical Reactivity under Vibrational Coupling to the Vacuum Electromagnetic Field. *Angewandte Chemie International Edition* **55,** 11462–11466 (2016).
57. Thomas, A. *et al.* Tilting a ground-state reactivity landscape by vibrational strong coupling. *Science* **363,** 615–619. ISSN: 10959203 (2019).
58. Lather, J., Bhatt, P., Thomas, A., Ebbesen, T. W. & George, J. Cavity catalysis by cooperative vibrational strong coupling of reactant and solvent molecules. *Angewandte Chemie International Edition* **58,** 10635–10638 (2019).
59. Hirai, K., Takeda, R., Hutchison, J. A. & Uji-i, H. Modulation of Prins Cyclization by Vibrational Strong Coupling. *Angewandte Chemie International Edition* **132,** 5370–5373 (2020).
60. Frisk Kockum, A., Miranowicz, A., De Liberato, S., Savasta, S. & Nori, F. Ultrastrong coupling between light and matter. *Nature Reviews Physics* **1,** 19–40 (2019).

61. De Liberato, S. Virtual photons in the ground state of a dissipative system. *Nature Communications* **8,** 1465. ISSN: 20411723 (2017).
62. De Liberato, S., Gerace, D., Carusotto, I. & Ciuti, C. Extracavity quantum vacuum radiation from a single qubit. *Physical Review A* **80,** 053810 (2009).
63. Stassi, R, Ridolfo, A, Di Stefano, O, Hartmann, M. & Savasta, S. Spontaneous conversion from virtual to real photons in the ultrastrong-coupling regime. *Physical review letters* **110,** 243601 (2013).
64. Vasanelli, A., Todorov, Y. & Sirtori, C. Ultra-strong light–matter coupling and superradiance using dense electron gases. *Comptes Rendus Physique* **17,** 861–873 (2016).
65. Liu, X. *et al.* Strong light–matter coupling in two-dimensional atomic crystals. *Nature Photonics* **9,** 30–34 (2015).
66. Dovzhenko, D., Ryabchuk, S., Rakovich, Y. P. & Nabiev, I. Light–matter interaction in the strong coupling regime: configurations, conditions, and applications. *Nanoscale* **10,** 3589–3605 (2018).
67. Chikkaraddy, R. *et al.* Single-molecule strong coupling at room temperature in plasmonic nanocavities. *Nature* **535,** 127–130 (2016).
68. Zengin, G. *et al.* Realizing strong light-matter interactions between single-nanoparticle plasmons and molecular excitons at ambient conditions. *Physical review letters* **114,** 157401 (2015).
69. Wang, S. *et al.* Coherent coupling of WS2 monolayers with metallic photonic nanostructures at room temperature. *Nano letters* **16,** 4368–4374 (2016).
70. Bitton, O., Gupta, S. N. & Haran, G. Quantum dot plasmonics: from weak to strong coupling. *Nanophotonics* **8,** 559–575 (2019).
71. Novotny, L. Strong coupling, energy splitting, and level crossings: A classical perspective. *American Journal of Physics* **78,** 1199–1202. ISSN: 0002-9505 (2010).
72. Gerry, C., Knight, P. & Knight, P. L. *Introductory quantum optics* (Cambridge university press, 2005).
73. Kaluzny, Y, Goy, P, Gross, M, Raimond, J. & Haroche, S. Observation of self-induced Rabi oscillations in two-level atoms excited inside a resonant cavity: The ringing regime of superradiance. *Physical review letters* **51,** 1175 (1983).
74. Schuster, D. *et al.* Resolving photon number states in a superconducting circuit. *Nature* **445,** 515–518 (2007).
75. Le Boité, A. Theoretical methods for ultrastrong light–matter interactions. *Advanced Quantum Technologies* **3,** 1900140 (2020).
76. Campos-Gonzalez-Angulo, J. A. & Yuen-Zhou, J. Polaritonic normal modes in transition state theory. *The Journal of Chemical Physics* **152,** 161101 (2020).
77. Campos-Gonzalez-Angulo, J. A., Ribeiro, R. F. & Yuen-Zhou, J. Resonant catalysis of thermally activated chemical reactions with vibrational polaritons. *Nature Communications* **10,** 4685 (2019).
78. Galego, J., Climent, C., Garcia-Vidal, F. J. & Feist, J. Cavity Casimir-Polder forces and their effects in ground-state chemical reactivity. *Physical Review X* **9,** 021057 (2019).
79. Di Stefano, O. *et al.* Resolution of gauge ambiguities in ultrastrong-coupling cavity quantum electrodynamics. *Nature Physics* **15,** 803–808 (2019).
80. Baranov, D. G. *et al.* Ultrastrong coupling between nanoparticle plasmons and cavity photons at ambient conditions. *Nature Communications* **11,** 2715. ISSN: 20411723 (2020).
81. Ciuti, C. & Carusotto, I. Input-output theory of cavities in the ultrastrong coupling regime: The case of time-independent cavity parameters. *Physical Review A* **74,** 033811 (2006).

82. Bisht, A. *et al.* Collective strong light-matter coupling in hierarchical microcavity-plasmon-exciton systems. *Nano letters* **19,** 189–196 (2018).
83. Todorov, Y. & Sirtori, C. Intersubband polaritons in the electrical dipole gauge. *Physical Review B* **85,** 045304. ISSN: 10980121. eprint: 1212.5140 (2012).
84. Huppert, S., Vasanelli, A., Pegolotti, G., Todorov, Y. & Sirtori, C. Strong and ultrastrong coupling with free-space radiation. *Physical Review B* **94,** 1–15. ISSN: 24699969. eprint: 1604.01668 (2016).
85. Canales, A., Baranov, D. G., Antosiewicz, T. J. & Shegai, T. Abundance of cavity-free polaritonic states in resonant materials and nanostructures. *The Journal of Chemical Physics* **154,** 024701 (2021).
86. Huttner, B. & Barnett, S. M. Quantization of the electromagnetic field in dielectrics. *Physical Review A* **46,** 4306–4322. ISSN: 10502947 (1992).
87. Antosiewicz, T. J., Apell, S. P. & Shegai, T. Plasmon–exciton interactions in a core–shell geometry: from enhanced absorption to strong coupling. *Acs Photonics* **1,** 454–463 (2014).
88. Guebrou, S. A. *et al.* Coherent emission from a disordered organic semiconductor induced by strong coupling with surface plasmons. *Physical review letters* **108,** 066401 (2012).
89. Gogna, R., Zhang, L. & Deng, H. Self-Hybridized, Polarized Polaritons in ReS2 Crystals. *ACS Photonics* **7,** 3328–3332 (2020).
90. Menghrajani, K. S. & Barnes, W. L. Strong coupling beyond the light-line. *ACS photonics* **7,** 2448–2459 (2020).
91. Bylinkin, A. *et al.* Real-space observation of vibrational strong coupling between propagating phonon polaritons and organic molecules. *Nature Photonics* **15,** 197–202 (2021).
92. Hu, F *et al.* Imaging propagative exciton polaritons in atomically thin WSe 2 waveguides. *Physical Review B* **100,** 121301 (2019).
93. Thomas, P. A., Menghrajani, K. S. & Barnes, W. L. Cavity-Free Ultrastrong Light-Matter Coupling. *The Journal of Physical Chemistry Letters* **12,** 6914–6918 (2021).
94. Kaeek, M., Damari, R., Roth, M., Fleischer, S. & Schwartz, T. Strong Coupling in a Self-Coupled Terahertz Photonic Crystal. *ACS Photonics* (2021).
95. Zhang, S. *et al.* Strong Exciton–Photon Coupling in Hybrid Inorganic–Organic Perovskite Micro/Nanowires. *Advanced Optical Materials* **6,** 1701032. ISSN: 21951071 (2018).
96. Evans, T. J. *et al.* Continuous-wave lasing in cesium lead bromide perovskite nanowires. *Advanced Optical Materials* **6,** 1700982 (2018).
97. Rao, A. *et al.* Microcavity-Like Exciton-Polaritons can be the Primary Photoexcitation in Bare Organic Semiconductors (2021).
98. Lather, J. & George, J. Improving Enzyme Catalytic Efficiency by Co-operative Vibrational Strong Coupling of Water. *The Journal of Physical Chemistry Letters* **12,** 379–384 (2020).
99. Imperatore, M. V., Asbury, J. B. & Giebink, N. C. Reproducibility of cavity-enhanced chemical reaction rates in the vibrational strong coupling regime. *The Journal of Chemical Physics* **154,** 191103 (2021).
100. Vergauwe, R. M. *et al.* Modification of enzyme activity by vibrational strong coupling of water. *Angewandte Chemie International Edition* **58,** 15324–15328 (2019).
101. Hiura, H., Shalabney, A. & George, J. Vibrational ultra strong coupling of water and ice (2019).

102. Li, T. E., Subotnik, J. E. & Nitzan, A. Cavity molecular dynamics simulations of liquid water under vibrational ultrastrong coupling. *Proceedings of the National Academy of Sciences* **117,** 18324–18331 (2020).
103. Giorgini, A., Avino, S., Malara, P., De Natale, P. & Gagliardi, G. Liquid droplet microresonators. *Sensors* **19,** 473 (2019).
104. Tampieri, F. & Tomasi, C. Size distribution models of fog and cloud droplets in terms of the modified gamma function. *Tellus* **28,** 333–347 (1976).
105. Best, A. Drop-size distribution in cloud and fog. *Quarterly Journal of the Royal Meteorological Society* **77,** 418–426 (1951).
106. Bai, Q., Perrin, M., Sauvan, C., Hugonin, J.-P. & Lalanne, P. Efficient and intuitive method for the analysis of light scattering by a resonant nanostructure. *Optics express* **21,** 27371–27382 (2013).
107. Doost, M. B., Langbein, W. & Muljarov, E. A. Resonant state expansion applied to two-dimensional open optical systems. *Physical Review A* **87,** 043827. ISSN: 10502947 (2013).
108. Castellanos-Gomez, A. *et al.* Deterministic transfer of two-dimensional materials by all-dry viscoelastic stamping. *2D Materials* **1,** 011002 (2014).
109. Shegai, T., Brian, B., Miljkovic, V. D. & Käll, M. Angular distribution of surface-enhanced Raman scattering from individual Au nanoparticle aggregates. *Acs Nano* **5,** 2036–2041 (2011).
110. Lieb, M. A., Zavislan, J. M. & Novotny, L. Single-molecule orientations determined by direct emission pattern imaging. *Journal of the Optical Society of America B* **21,** 1210. ISSN: 0740-3224 (2004).